

The *Spitzer* search for the transits of HARPS low-mass planets - II. Null results for 19 planets^{*}

M. Gillon¹, B.-O. Demory^{2,3}, C. Lovis⁴, D. Deming⁵, D. Ehrenreich⁴, G. Lo Curto⁶, M. Mayor⁴, F. Pepe⁴,
D. Queloz^{3,4}, S. Seager⁷, D. Ségransan⁴, S. Udry⁴

¹ Space sciences, Technologies and Astrophysics Research (STAR) Institute, Université de Liège, Allée du 6 Août 17, Bat. B5C, 4000 Liège, Belgium

² University of Bern, Center for Space and Habitability, Sidlerstrasse 5, CH-3012, Bern, Switzerland

³ Cavendish Laboratory, J. J. Thomson Avenue, Cambridge CB3 0HE, UK

⁴ Observatoire de Genève, Université de Genève, 51 Chemin des Maillettes, 1290 Sauverny, Switzerland

⁵ Department of Astronomy, University of Maryland, College Park, MD 20742-2421, USA

⁶ European Southern Observatory, Karl-Schwarzschild-Str. 2, D-85478 Garching bei München, Germany

⁷ Department of Earth, Atmospheric and Planetary Sciences, Department of Physics, Massachusetts Institute of Technology, 77 Massachusetts Ave., Cambridge, MA 02139, USA

Received date / accepted date

ABSTRACT

Short-period super-Earths and Neptunes are now known to be very frequent around solar-type stars. Improving our understanding of these mysterious planets requires the detection of a significant sample of objects suitable for detailed characterization. Searching for the transits of the low-mass planets detected by Doppler surveys is a straightforward way to achieve this goal. Indeed, Doppler surveys target the most nearby main-sequence stars, they regularly detect close-in low-mass planets with significant transit probability, and their radial velocity data constrain strongly the ephemeris of possible transits. In this context, we initiated in 2010 an ambitious *Spitzer* multi-Cycle transit search project that targeted 25 low-mass planets detected by radial velocity, focusing mainly on the shortest-period planets detected by the HARPS spectrograph. We report here null results for 19 targets of the project. For 16 planets out of 19, a transiting configuration is strongly disfavored or firmly rejected by our data for most planetary compositions. We derive a posterior probability of 83% that none of the probed 19 planets transits (for a prior probability of 22%), which still leaves a significant probability of 17% that at least one of them does transit. Globally, our *Spitzer* project revealed or confirmed transits for three of its 25 targeted planets, and discarded or disfavored the transiting nature of 20 of them. Our light curves demonstrate for *Warm Spitzer* excellent photometric precisions: for 14 targets out of 19, we were able to reach standard deviations that were better than 50ppm per 30 min intervals. Combined with its Earth-trailing orbit, which makes it capable of pointing any star in the sky and to monitor it continuously for days, this work confirms *Spitzer* as an optimal instrument to detect sub-mmag-deep transits on the bright nearby stars targeted by Doppler surveys.

Key words. binaries: eclipsing – planetary systems – stars: individual: BD-061339, HD 1461, HD 10180, HD 13808, HD 20003, HD 20781, HD 31527, HD 39194, HD 45184, HD 47186, HD 51608, HD 93385, HD 96700, HD 115617, HD 125612, HD 134060, HD 181433, HD 215497, HD 219828 - techniques: radial velocity - techniques: photometric

1. Introduction

Starting from 2004 (Butler et al. 2004, Santos et al. 2004), exoplanet search projects have been detecting planets of a few to ~ 20 Earth masses at an ever-increasing rate, revealing them to be very frequent around solar-like stars (e.g. Howard et al. 2012) where they tend to form compact multiple systems (Rowe et al. 2014). Based on their mass (or minimal mass for planets detected by radial velocity - RV), these objects are loosely classified as super-Earths ($M_p \leq 10M_\oplus$) and Neptunes ($M_p > 10M_\oplus$). This division is based on the theoretical limit for the runaway accretion of H/He by a protoplanet, $\sim 10M_\oplus$ (Rafikov 2006),

and thus implicitly assumes that Neptunes are predominantly ice giants and that most super-Earths are massive terrestrial planets. However, the growing sample of transiting low-mass exoplanets with precise mass and radius measurements exhibit a wide diversity of densities that reveals a very heterogeneous population, making simplistic inferences hazardous when based on the comparison with solar system planets. A better understanding of this ubiquitous class of planets requires the thorough characterization of a significant sample, not only the precise measurements of their physical dimensions but also the exploration of their atmospheric composition to alleviate the strong degeneracies of composition models in this mass range (e.g. Seager et al. 2007, Valencia et al. 2013).

Among the known transiting low-mass planets, GJ 436 b (Butler et al. 2004, Gillon et al. 2007) and GJ 1214 b (Charbonneau et al. 2009) are the most thoroughly characterized planets in the Neptune and super-Earth mass

Send offprint requests to: michael.gillon@ulg.ac.be

^{*} The photometric and radial velocity time series used in this work are only available in electronic form at the CDS via anonymous ftp to cdsarc.u-strasbg.fr (130.79.128.5) or via <http://cdsweb.u-strasbg.fr/cgi-bin/qcat?J/A+A/>

ranges, respectively, thanks to the small size (~ 0.45 and $0.2 R_{\odot}$) and proximity (about a dozen of pc) of their M-dwarf host stars. First constraints on their atmospheric properties have indeed been obtained by several programs (e.g. Kreidberg et al. 2014, Knutson et al. 2014a, Ehrenreich et al. 2015). Extending this kind of detailed studies to Neptunes and super-Earths orbiting solar-type hosts requires the detection of such planets in transit in front of extremely bright and nearby stars. A straightforward method to achieve this goal is to search for the transits of the low-mass planets detected by RV surveys. Indeed, these surveys target the most nearby main-sequence stars, and they have now detected enough short-period low-mass planets to make it highly probable that a handful of them transit their parent stars, as demonstrated by the previous detections by the MOST space telescope of the transits of the super-Earths 55 Cnc e (Winn et al. 2011)¹. Thanks to the brightness of their host stars, the atmospheric characterization of these two planets has already started (e.g. Demory et al. 2012, Knutson et al. 2014b). More recently, the same approach enabled us to reveal with *Spitzer* the transiting configuration of the rocky planet HD 219134 b (Motalebi et al. 2015) which, at 6.5pc, is the nearest known transiting exoplanet.

Searching for the transits of RV low-mass planets is one of the main objectives of the future European space mission CHEOPS (Broeg et al. 2013). However, CHEOPS is not due to launch before the end of 2017. To set it on its path, back in 2010 we set up an ambitious project using *Spitzer*/IRAC (Fazio et al. 2004) to search for the transits of the RV low-mass planets that have the highest geometric transit probabilities, focusing mainly on the shortest-period planets detected by the HARPS spectrograph (Mayor et al. 2003). Our *Spitzer* transit search was composed of a cryogenic program targeting HD 40307 b (ID 495, 27.5hr), and three so-called *Warm* (i.e. non cryogenic) programs (ID 60027, 90072, and 11180; 100hr, 300hr, and 9.5hr) that targeted 24 other RV low-mass planets. Its published results have so far been the non-detection of the transits of HD 40307 b (Gillon et al. 2010, hereafter G10) and GJ 3634 b (Bonfils et al. 2011), the detection and confirmation of the transits of 55 Cnc e (Demory et al. 2011, Gillon et al. 2012a), the confirmation of the transiting nature of HD 97658 b (Van Grootel et al. 2014), and the detection of a transit of HD 219134 b (Motalebi et al. 2015). Results for another planet will be presented in a forthcoming paper (Ségransan et al., in prep.) We report here null results for the 19 other targets of the project.

We first present our targets and our determination of their transit ephemeris. In Sect. 3, we present our *Spitzer* data and their reduction. Section 4 describes our data analysis. Its main results are presented in Sect. 5. Finally, we discuss our global results and give our conclusions in Sect. 6.

2. Targets and transit ephemeris determination

Table 1 and Tables A.1 to A.4 list the 19 targets of this work. For each target, we performed an analysis of the available RVs, including new measurements for some of them

gathered by HARPS², to derive the most accurate transit ephemeris. This analysis was done with the adaptative Markov Chain Monte-Carlo (MCMC) algorithm described in G10 (see also Gillon et al. 2012a, 2012b, 2014). Our nominal model was based on a star and one or several planets on Keplerian orbits around their common center of mass. For some cases, we added a linear or quadratic trend to the model, based on the minimization of the Bayesian information criterion (BIC, Schwarz 1974) to elect our final model. We checked that planet-planet interactions had negligible influence on our solutions, using, for this purpose, the *Systemic Console* software (Meschiari et al. 2009). We also used this software to perform an initial optimization of parameters to check that no solution existed with a higher likelihood than the published one. During this initial stage of the analysis, the RV errors were assumed to be measurement uncertainties. Once this initial stage was completed, we measured the quadrature difference between the rms of the residuals and the mean error, and this "jitter noise" (Wright 2005) was quadratically summed to the measurement uncertainties. We then performed a MCMC analysis to probe the posterior probability distribution functions (PDF) of the model and physical parameters

Each MCMC analysis was composed of five Markov chains of 10^5 steps, the first 20% of each being considered as its burn-in phase and discarded. For each run, the convergence of the five Markov chains was checked using the statistical test of Gelman & Rubin (1992). The resulting posterior PDFs for the transit time and period were then used to schedule the *Spitzer* observations, with monitoring the $2 - \sigma$ transit window as the goal, i.e. keeping the probability to miss a transit below 5%.

Even if the resulting posterior PDFs for the orbital eccentricity of most target planets were compatible with zero, we did not assume a purely circular orbit for them to ensure the reliability of our derived transit ephemeris. Indeed, several examples of low-mass exoplanets with significantly eccentric few-days orbits (e.g. GJ 436 b, HAT-P-11 b, HD215497 b) remind us of the risks of systematically assuming circular orbits for close-in exoplanets based on tidal circularization arguments. An established theory for tidal dissipation mechanisms is still a long-term goal, and reaching it relies mostly on gathering new observational constraints.

Once the *Spitzer* observations had been performed for a planet, we made a second MCMC analysis of the most up-to-date RV dataset, this time with the fitted transit time corresponding to the epoch covered by the *Spitzer* run. The purpose of this analysis was to derive the most accurate orbital parameters, transit ephemeris, and minimal masses for the planets under consideration. Indeed, for most of them HARPS gathered a significant number of RV measurements between the scheduling of the *Spitzer* observations and the final analysis of the *Spitzer* images.

Tables A.1 to A.4 present the results obtained for each targeted planet from these MCMC analyses of the most up-to-date RV dataset. In addition to some basic parameters for the host stars, these tables give the origin of the RVs used as input in our MCMC analysis for each target, and provide the most relevant results of our MCMC analysis:

¹ Our *Spitzer* program independently revealed the transiting nature of 55 Cnc e (Demory et al. 2011). and HD 97658 b (Dragomir et al. 2013)

² Most HARPS measurements used in this work are available on the ESO/HARPS online archive at <http://archive.eso.org/wdb/wdb/eso/repro/form>

the transit and occultation ephemeris, the minimal mass, the expected minimum transit depth corresponding to a pure iron planet (Seager et al. 2007), the equilibrium day-side temperature, the orbital parameters, and the expected duration for a central transit. The radius of the star was derived from the luminosity and effective temperature, taking bolometric corrections from Flower (1996).

Tables A.1 to A.4 also present the median value and the 1- σ errors for the prior transit probability. It was computed at each step of the MCMC with the following formula:

$$P(tr) = \left(\frac{R_*}{a}\right) \left(\frac{1 + e \sin \omega}{1 - e^2}\right), \quad (1)$$

where R_* is the stellar radius, a is the orbital semi-major axis, e is the orbital eccentricity and ω is the argument of periastron. This probability estimate does not take into account that planets are more likely to be discovered by RV if their orbit is significantly inclined (e.g. Wisniewski et al. 2012). By performing Bayesian simulations that assume different prior PDFs for the planetary masses, Stevens & Gaudi (2013) have shown that this bias increases the transit probability of short-period low-mass RV planets like the ones considered here by only $\sim 20\%$ in average. Furthermore, its actual estimation for a given planet depends strongly on the assumed prior PDFs for the planetary masses. We have thus neglected it in the context of this work.

3. *Warm Spitzer* photometry

Tables A.5 to A.11 provide a summary of the *Spitzer* observations. Since all our targets are very bright (K between 2.96 and 6.90), all of them were observed in subarray mode (32x32 pixels windowing of the detector), the extremely fast Fowler sampling (~ 0.01 s), which maximizes the duty cycle and signal-to-noise ratio (S/N). No dithering pattern was applied to the telescope (continuous staring). For each target, the exposure time was selected to maximize the S/N while staying in the linear regime of the detector, basing on the *Warm Spitzer* flux density estimator tool³ and on the instructions of the *Warm Spitzer* Observer Manual⁴.

The observations of program 60027 (Cycle 6) and 90072 (Cycle 9) were performed between 2009 Dec 14 and 2010 Sep 11, and between 2012 Dec 03 and 2014 May 14, respectively. For several of the Cycle 9 targets, we benefitted from the newly introduced PCRS peak-up mode (Ingalls et al. 2012). This mode provides enhanced accuracy in the position of the target on the detector, to a significant decrease of the so-called ‘pixel phase effect’ that is the most important source of correlated noise in high-S/N staring mode observation with IRAC InSb arrays (e.g. Knutson et al. 2008). For HD 1461 b, we supplemented our data with the IRAC 4.5 μ m observations presented by Kammer et al. (2014), as described in Sect. 5.2.

On a practical level, each observation run was divided in one or several science astronomical observational requests (AOR) of 12hr at most, preceded by a short (20-30 min) AOR to allow the pointing of the telescope and the instrument to stabilize. The IDs of all AORs are given for each

target in Tables A.5 to A.11. These tables also give the version of the *Spitzer* pipeline used to calibrate the corresponding images, the resulting files being called basic calibrated data (BCD) in the *Spitzer* nomenclature. Each subarray mode BCD is composed of a cube of 64 subarray images of 32x32 pixels (pixel scale = 1.2 arc second).

The following reduction strategy was used for all the *Spitzer* AOR. We first converted fluxes from the *Spitzer* units of specific intensity (MJy/sr) to photon counts, then aperture photometry was performed on each subarray image with the IRAF/DAOPHOT⁵ software (Stetson, 1987). For each AOR, we tested different aperture radii and background annuli, and selected the combination minimizing the white and red noises in the residuals of a short data fitting analysis. The center and width of the point-spread functions (PSF) were measured by fitting a 2D-Gaussian profile on each image. The $x - y$ distribution of the measurements was then studied, and measurements that had a visually discrepant position relative to the bulk of the data were then discarded. For each block of 64 subarray images, we then discarded the discrepant values for the measurements of flux, background, x - and y -positions using a 10- σ median clipping for the four parameters, and the resulting values were averaged, the photometric errors being taken as the errors on the average flux measurements. Finally, a 50- σ slipping median clipping was used on the resulting light curves to discard outliers (owing to, for example, cosmic hits).

4. Global *Warm Spitzer* + RV data analysis

We analyzed the *Spitzer* photometric time-series supplemented by the RVs with our MCMC code. For each target, our model for the RVs was the same as the one presented in Sect. 2. The assumed photometric model consisted of the eclipse model of Mandel & Agol (2002) to represent the possible eclipses of the probed planets, multiplied for each light curve by a baseline model that aimed to represent the other astrophysical and instrumental effects at the source of photometric variations. We assumed a quadratic limb-darkening law for the stars. For each light curve that corresponded to a specific AOR, we based the selection of the baseline model on the minimization of the BIC. Tables A.5 to A.11 present the baseline function elected for each AOR.

Following Gillon et al. (2014), the instrumental models included three types of low-order polynomials. The first one had as variables the x - and y -positions of the center of the PSF to represent the so-called pixel phase effect of the IRAC InSb arrays (e.g. Knutson et al. 2008). The second one had the PSF widths in the x - and/or the y -direction as variables, its inclusion in the baseline model strongly increasing the quality of the fit for all AORs (the so-called PSF breathing effect, see also Lanotte et al. 2014). The third function was a polynomial of the logarithm of time to represent a sharp increase of the detector response at the start of some AORs (the so-called ramp effect, Knutson et al. 2008). To improve the quality of the modeling of the pixel phase effect, especially the fitting of its highest fre-

³ <http://ssc.spitzer.caltech.edu/warmmission/propkit/pet/starpd>

⁴ <http://ssc.spitzer.caltech.edu/warmmission/propkit/som>

⁵ IRAF is distributed by the National Optical Astronomy Observatory, which is operated by the Association of Universities for Research in Astronomy, Inc., under cooperative agreement with the National Science Foundation.

quency components, for most AORs we supplemented the x - and y -polynomial with the bi-linearly-interpolated sub-pixel sensitivity (BLISS) mapping method (Stevenson et al. 2012). The sampling of the position space was selected so that at least five measurements fall within the same sub-pixel. See Gillon et al. (2014) for more details.

The jump parameters of the MCMC, i.e. the parameters randomly perturbed at each step of the Markov Chains, were as follows:

- The stellar mass M_* , radius R_* , effective temperature T_{eff} , and metallicity [Fe/H]. For these four parameters, normal prior PDFs were assumed based on the values given in Tables A.1-4.
- For the potential transiting planet, the parameter $b' = a \cos i / R_*$, where a is the orbital semi-major axis and i is the orbital inclination. b' would correspond to the transit impact parameter in the case of a circular orbit. The step was rejected if $b' > a / R_*$. For the other planets of the system, b' was fixed to 0.
- The parameter $K_2 = K \sqrt{1 - e^2} P^{1/3}$ for all planets of the system, K being the RV orbital semi-amplitude, e the orbital eccentricity, and P the orbital period.
- The orbital period P of each planet.
- For each planet, the two parameters $\sqrt{e} \cos \omega$ and $\sqrt{e} \sin \omega$, e being the orbital eccentricity and ω being the argument of periastron.
- The planet/star area ratio $dF = (R_p / R_*)^2$ for the potential transiting planet. At each step of the MCMC, the planetary radius corresponding to a pure iron composition was computed under the formalism given by Seager et al. (2007), and if the planetary radius derived from dF and R_* was smaller, the step was rejected. A similar rejection was done for $R_p > 11R_{\oplus}$, an implausibly large size for the low-mass planets considered here. The goal of these prior constraints on R_p was to avoid fitting extremely shallow transits and ultra-grazing transits of unrealistically big planets in the correlated noise of the light curves to ensure an unbiased posterior transit probability. For the other planets of the multiple systems, dF was fixed to 0. In all cases, we checked that a transit of another planet of these systems was not expected to occur during the *Spitzer* observations.
- The time of inferior conjunction T_0 for all planets of the system. For the potential transiting planets that we considered, T_0 corresponds approximatively to the mid-time of the transit searched for by *Spitzer*.

The limb-darkening of the star was modeled by a quadratic law (Claret 2000). For both *Warm Spitzer* band-passes (3.6 and 4.5 μm), values for the two quadratic limb-darkening coefficients u_1 and u_2 were drawn at each step of the MCMC from normal distributions whose expectations and standard deviations were drawn from the tables of Claret & Bloemen (2011) for the corresponding band-passes and for the stellar atmospheric parameters given in Tables A.1-4.

Five chains of 100000 steps were performed for each analysis, their convergences being checked using the statistical test of Gelman and Rubin (1992). They followed a preliminary chain of 100000 steps, which was performed to estimate the need to rescale the photometric errors. For each light curve, the standard deviation of the residuals was then compared to the mean photometric errors, and the resulting ratios β_w were stored. β_w represents the under-

overestimation of the white noise of each measurement. On its side, the red noise present in the light curve (i.e. the inability of our model to represent perfectly the data) was taken into account as described in G10, i.e. a scaling factor β_r was determined from the standard deviations of the binned and unbinned residuals for different binning intervals ranging from 5 to 120 minutes, the largest values being kept as β_r . At the end, the error bars were multiplied by the correction factor $CF = \beta_r \times \beta_w$. The derived values for β_r and β_w are given for each light curves in Tables A.5-11.

5. Results

For each planet searched for transit, Table 1 presents the derived posterior full transit probability $P(f, D)$, i.e. the probability that the planet undergoes full transits given the *Spitzer* data. Bayes theorem shows that

$$P(f, D) = \frac{P(f)P(D, f)}{P(f)P(D, f) + P(g)P(D, g) + P(n)P(D, n)} \quad (2)$$

$P(f)$, $P(g)$, and $P(n)$ are the prior (geometric) probabilities of full, grazing and no transit, respectively ($P(g)$ is close to zero, and $P(n) \sim 1 - P(f)$). $P(D, f)$, $P(D, g)$, and $P(D, n)$ are the probabilities (likelihoods) to have the observed data given the three mutually exclusive hypotheses. All the terms of the right-hand side of Eq. 2 are probed by the MCMC analysis, resulting in accurate estimates of $P(f, D)$.

Figs. 1-4, 6-14, and 16-20 show the resulting detrended *Spitzer* light curves and the derived posterior PDFs for the inferior conjunction. Below, we provide relevant details for our 19 targets.

5.1. BD-061339

BD-061339 (a.k.a. GJ 221) is a V=9.7 late-K dwarf around which two planets were detected by HARPS (Lo Curto et al. 2013), a super-Earth on a $\sim 3.9\text{d}$ orbit and a planet of $\sim 50M_{\oplus}$ minimal mass on a $\sim 126\text{d}$ orbit. Our model selection process for the RVs (HARPS + PFS) favored a model with a slope in addition to these two planets (Table A.1). The derived value for this slope is $-0.73 \pm 0.15 \text{ ms}^{-1}$ per year, which could correspond to a giant planet in outer orbit or to the imprint of a stellar magnetic cycle.

As can be seen in Fig. 1, the high-precision of the *Spitzer* photometry (42 ppm per 30 min time bin) discards any transit for BD-061339 b during our observations, even for an unrealistic pure iron composition. However, the edge of the right wing of the PDF for T_0 was not explored by our observations, so a late transit is still possible. The resulting posterior full transit probability is 0.53% (Table 1), high enough to justify a future exploration of the late part of the transit window.

5.2. HD 1461

HD 1461 is a V=6.5 solar-type star known to host a super-Earth on a 5.77d orbit (Rivera et al. 2010). Recently, a second super-Earth on a 13.5d orbit was announced by Díaz et al. (2015). In our analysis of the HARPS + Keck RVs for this star, the convergence of the MCMC appeared to be significantly improved by removing the 20 first Keck

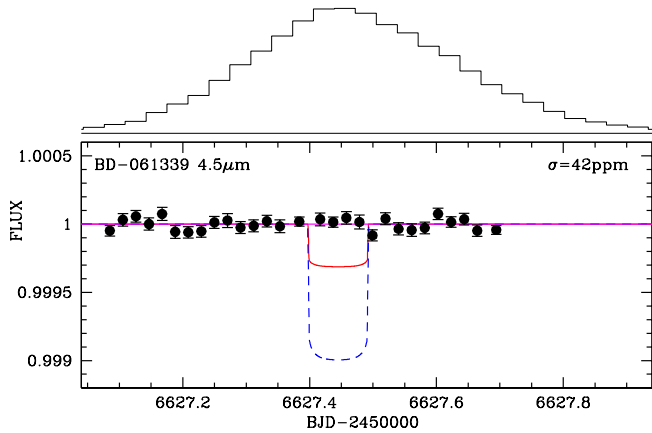


Fig. 1. *Warm Spitzer* photometry for BD-061339 after correction for the instrumental effects, normalization, and binning per 30 min. Models for a central transit of BD-061339 b are shown, assuming a pure iron (red solid line) and pure water ice (blue dashed line) composition. The highest posterior probability model, which assumes no transit, is also shown (purple line). The posterior PDF for the transit timing derived from the RV analysis is shown above the figure.

measurements for which the exposure time and the resulting precision were significantly lower than for the rest of the data. Our analysis favored a three planet model (5.77, 13.5, and 377 days period) in addition to a second-order time polynomial, suggesting the presence of a fourth low-frequency signal, and an activity model consisting of a sum of second-order polynomials in the cross-correlation function (CCF, Baranne et al. 1996, Queloz et al. 2001) parameters (Table A.1): width, contrast, and bisector. We inferred that the 377d period, close to the duration of a year, is caused by a systematic effect (the stitching) recently revealed to affect HARPS data (Dumusque et al. 2015). The data used by Díaz et al. (2015) were corrected for this effect. We made several tests that showed that the inclusion or not of this 377d Doppler signal in the RV model did not affect the results for the closest-in planet, including its transit ephemeris, so we kept it in our final analysis.

A search for a transit of HD 1461 b with *Spitzer* was presented by Kammer et al. in 2014 (program 80220). We first reduced their data and used them with the HARPS+Keck RVs as input for a global MCMC analysis. The resulting posterior full transit probability was 0.5%, suggesting that a small but significant fraction of the transit window was not covered by these *Spitzer* observations. As can be seen in Fig. 2, a transit that had ended just before the *Spitzer* observations remained possible. This possibility is amplified by the ramp effect that affected the first hour of the *Spitzer* data, resulting in an increase of brightness that could be degenerated with a transit egress. We thus complemented these *Spitzer* archive data with new *Spitzer* observations covering the first part of the transit window. We performed a global analysis of all *Spitzer* + RVs that made a transiting configuration for HD 1461 b very unlikely (see Fig. 2), the resulting posterior full transit probability now being of only 0.14% (Table 1).

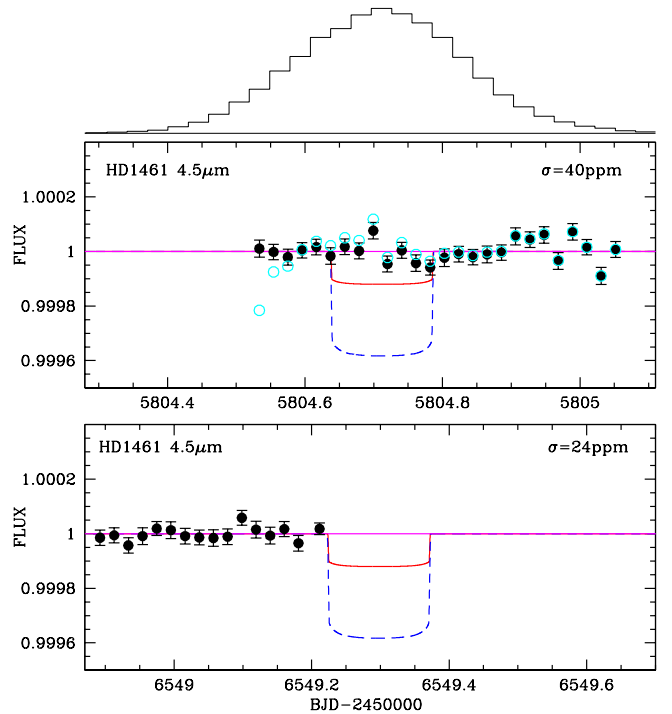


Fig. 2. Same as Fig. 1 for HD 1461 b. Upper panel corresponds to archive data (program 80220, Kammer et al. 2014), and the lower panel corresponds to the new data gathered in our program 90072. The upper panel also shows the light curve derived without correction of the ramp effect (open pale green circles).

5.3. HD 10180

HD 10180 is a $V=7.3$ solar-type star hosting a particularly interesting system of six planets of relatively low-masses (Lovis et al. 2011). At first, we did not consider searching for the transit of the 1.18d-period Earth-mass planet candidate HD 10180 b presented by Lovis et al. (2011) because its Doppler detection was not firmly secured when we planned our *Spitzer* Cycle 6 observations of the star. Furthermore, we estimated that its transit would, in any case, be too shallow (a few dozens of ppm, at most 100 ppm) to be firmly detected with *Spitzer*. We thus focused on the planet HD 10180 c ($M \sin i = 13M_{\oplus}$, $P = 5.76$ d), for which the Doppler signal was clearly detected in the HARPS data, and for which the expected transit depth (> 150 ppm) was large enough to ensure a sure detection with *Spitzer*. enabled us to discard a transit of the planet (Fig. 3), the resulting posterior full transit probability being of 0.14% (Table 1). Still, we noticed a shallow structure in the detrended photometry that occurs at a time consistent with a transit of HD 10180 b (Fig. 4), the best-fit transit depth of ~ 90 ppm translating into a radius of $1.2 R_{\oplus}$ consistent with a planetary mass of $1M_{\oplus}$. Based on this result, we decided to observe in our Cycle 9 program 90072 two more transit windows of HD 10180 b, this time at $4.5 \mu\text{m}$. No transit structure was clearly detected in the resulting light curves (Fig. 4, bottom), and a short MCMC analysis of the data led us to conclude that these new data do not increase the significance of the 2010 tentative detection. We thus conclude that the low-amplitude structure in

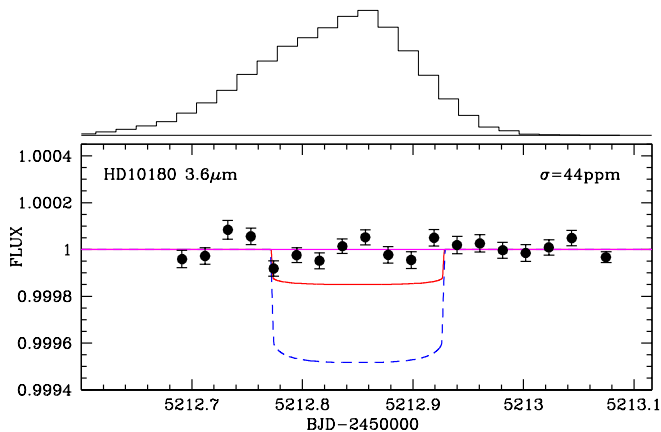


Fig. 3. Same as Fig. 1 for the light curve of 2010 Jan 16 for HD 10180 c.

our Cycle 6 *Spitzer* light curve is probably just correlated noise of instrumental origin that is not perfectly represented by our baseline model and that can easily be modeled by a shallow enough transit profile. For *Spitzer*, the average amplitude of these correlated noise structures is of a few dozen of ppm (see Sec. 6), making the firm detection of a unique transit shallower than ~ 100 ppm impossible - similarly to the one expected for HD 10180 b (see discussion in Sec. 6 and our estimated detection thresholds in Table 1). This so-called red noise limit can be surpassed, but only by gathering more observations of the transit window, as we did here (see also the case of HD 40307 b in Gillon et al. 2010).

5.4. HD 13808

In 2012, we analyzed the HARPS dataset for the $V=8.4$ early K-dwarf HD 13808, confirming the existence of the two planets around it with periods of 14.2 d and 53.7 d announced by Mayor et al. (2011, hereafter M11). Furthermore, our analysis revealed the existence of (1) a low-frequency signal that was well-modeled with a quadratic trend, whose origins is the magnetic cycle of the star (Queloz et al. in prep.), and (2) a low-amplitude Doppler signal with a period of 1.091 d which corresponds to a planet of $M_p \sin i = 1.5 \pm 0.3 M_\oplus$ with an interestingly high transit probability of $\sim 20\%$. The false-alarm probability (FAP) derived by *Systemic* for this short-period planet candidate was close to 1%. Based on this small FAP and the scientific importance of this putative planet if transiting, we decided to monitor two of its transit windows with *Spitzer*. Unfortunately, the resulting light curves did not show any convincing transit-like structure (Fig. 5). Our *Spitzer* data were not acquired during a transit window of the planet at 14.2 d, thus keeping its transiting nature unconstrained.

In 2014, we analyzed the updated HARPS dataset. This analysis confirmed the existence of the low-frequency signal of magnetic cycle origins, still well-modeled by a quadratic trend, but it led to a much lower significance (FAP $\sim 10\%$) for the 1.091 d signal. A stronger signal at 18.98 d and at its alias period of 1.056 d emerged with FAP close to 1%. Still, including a polynomial function of the CCF parameters (bisector, contrast, width) in our MCMC modeling,

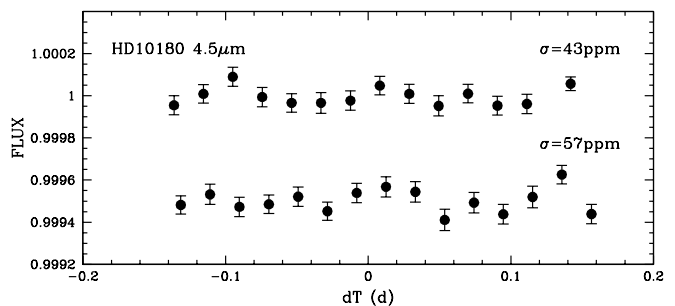
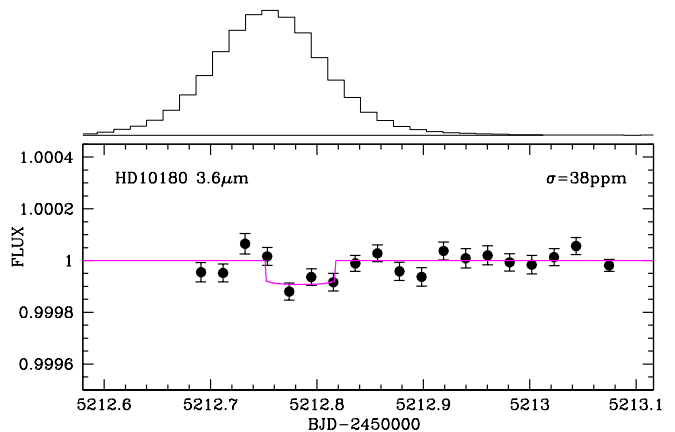


Fig. 4. *Top:* Same as Fig. 3, except that a possible transit of HD 10180 b was included in the global model. Highest posterior probability transit model for HD 10180 b is shown in purple. The posterior PDF for the transit timing of HD 10180 b derived from an RV analysis assuming 7 planets is shown above the figure. *Bottom:* 2013 *Warm Spitzer* photometry for HD 10180 binned per 30 min, corrected for the instrumental effects, normalized, and folded on the transit ephemeris for HD 10180 b based on our tentative detection of a transit and on the results of an RV analysis assuming 7 planets (dT = time from most likely mid-transit time).

these signals vanished from the residuals, indicating that their origin is stellar (activity), not planetary. The period 18.98 d could then be interpreted as the rotation period of the star, resulting in an equatorial rotation speed $\sim 2.2 \text{ km.s}^{-1}$ which is consistent with the measured $v \sin i$ of 2 km.s^{-1} (Glebocki & Gnacinski 2005). This stellar signal, combined with aliasing effects, would thus be responsible for creating spurious signals with periods slightly larger than 1 d.

5.5. HD 20003

HD 20003 is a late-G dwarf of magnitude $V=8.4$ for which M11 announced the detection by HARPS of two planets with periods of 11 d and 33 d. Our analysis of the updated HARPS dataset for HD 20003 not only confirmed these planets, but also revealed two longer period signals: one at ~ 180 d that was determined as originating from the stitching effect, and another, at ~ 10 yr, that originates from the magnetic cycle of the star (Udry et al. in prep.). Only HD 20003 b ($P=11$ d) has a significantly eccentric orbit. We used *Spitzer* to probe its transiting nature. We did not de-

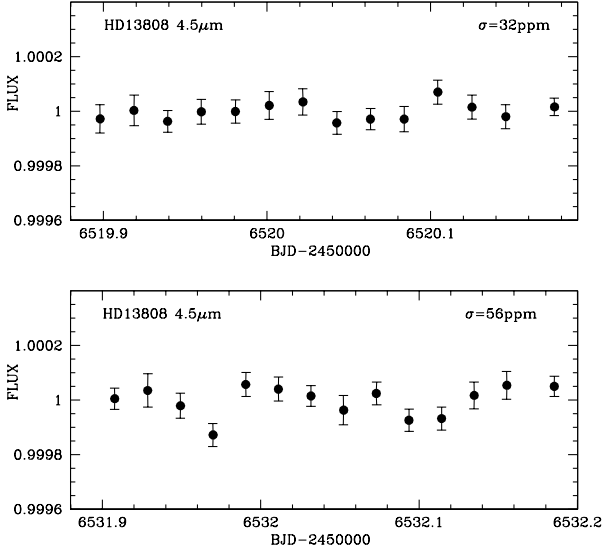


Fig. 5. Same as Fig. 1 for HD 13808 b. These data probed the $2\text{-}\sigma$ transit window of a planetary candidate that turned out to be a spurious signal with more RV data (see Sec. 5.4 for details).

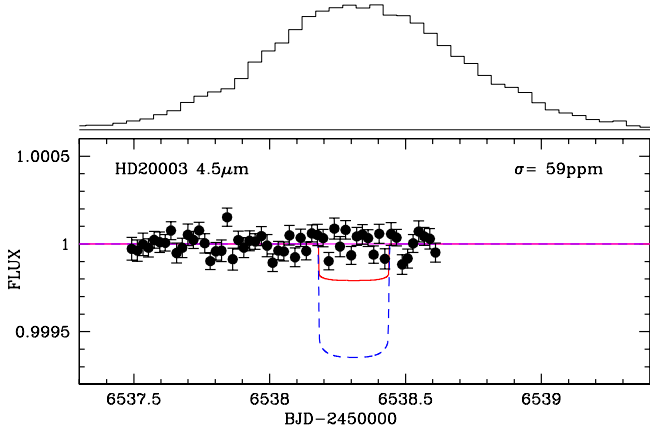


Fig. 6. Same as Fig. 1 for HD 20003 b.

tect a transit (Fig. 6). But, as can be seen in Fig. 6, we did not probe the latest part of its transit window, resulting in a small but still significant posterior full transit probability of 0.54% (Table 1).

5.6. HD 20781

Based on 96 HARPS measurements, M11 announced the discovery of two Neptunes with orbital periods of 29.1 d and 85.1 d around this nearby $V=8.4$ K0-dwarf. The analysis of our much extended HARPS dataset (212 points) confirmed the existence of these two planets, while revealing the existence of two super-Earths in shorter orbits: a $M_p \sin i = 6.3M_\oplus$ planet at 13.9 d period, and a $M_p \sin i = 2.1M_\oplus$ planet at 5.3 d period (Udry et al. in prep.). The low minimal mass and relatively high transit probability ($>7\%$) of this latter planet made it an espe-

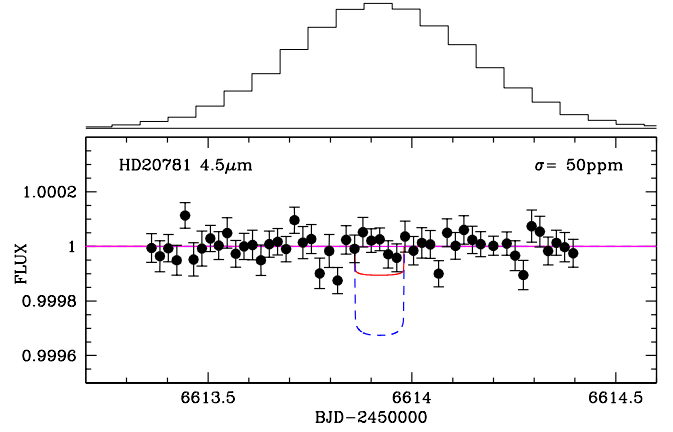


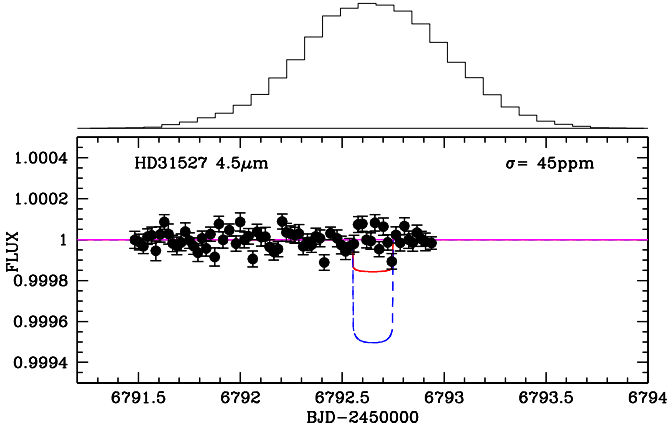
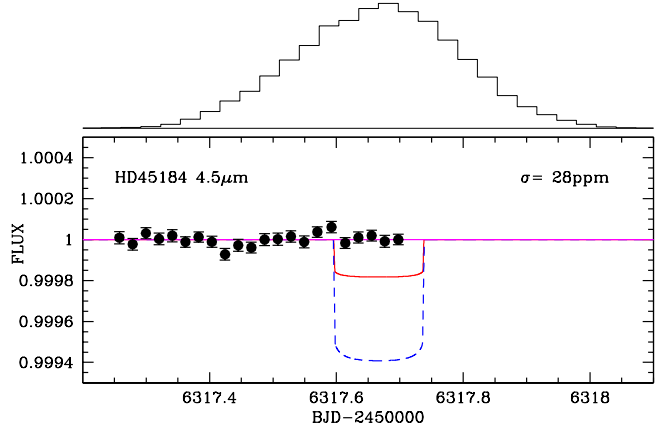
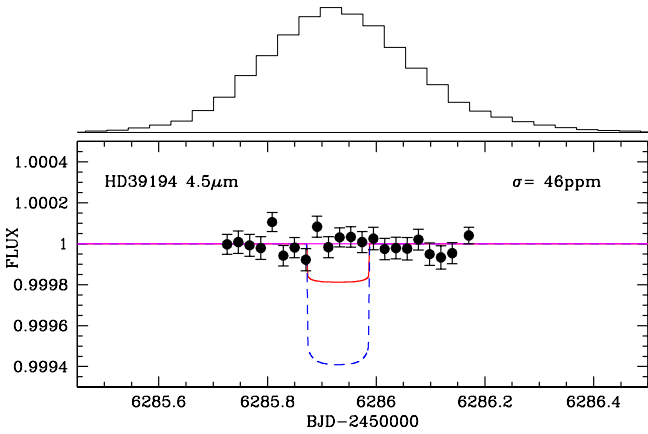
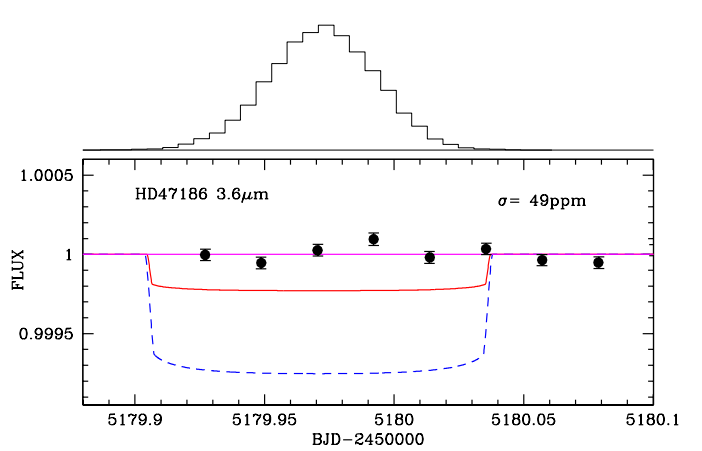
Fig. 7. Same as Fig. 1 for HD 20781 b.

cially interesting target for a transit search, so we included it in the target list of our *Spitzer* program and observed one of its transit window during Cycle 9. Because of the extreme faintness of the Doppler signal ($K \sim 90 \text{ cm.s}^{-1}$), the orbital eccentricity of the planet is poorly constrained from the RVs alone, resulting in a particularly large transit window. As such, we assumed the orbit to be circular to minimize the required *Spitzer* time, judging a circular orbit as a reasonable assumption, taking into consideration the strong tidal forces exerted by the star at such close distance and the compactness of the planetary system that would make any significantly eccentric orbit unstable.

Our *Spitzer* photometry did not reveal any transit-like structure (Fig. 7), the resulting posterior full transit probability being 0.15% (Table 1). Still, our precision is not high enough to securely detect the transit of this very low-mass planet if its amplitude is below $\sim 150\text{ppm}$, corresponding to Mercury-like iron-rich compositions. Re-observing the planet’s transit window at higher precision with, for example, CHEOPS will be mandatory to fully exclude a transiting configuration for the planet.

5.7. HD 31527

M11 announced the existence of three Neptune-mass planets around this nearby $V = 7.5$ solar-type star, with orbital periods of 16.5 d, 51.3 d, and 275 d. Our analysis of the extended HARPS dataset (242 vs 167 measurements) confirmed the existence of these planets and improved their orbital parameters, while not revealing any other planet (Udry et al. in prep.). We used ~ 36 hr of continuous *Spitzer* observation to search for a transit of the innermost planet, HD 31527 b (geometric transit probability = 4.4%). The resulting light curve did not reveal any transit (Fig. 8), the resulting posterior full transit probability being of 0.45% (Table 1). Compared to the orbital solution that we used to schedule our *Spitzer* observations, the updated solution presented here (Table 2) results in *Spitzer* observations that are not well centered on the peak of the posterior PDF for the transit timing. The right wing of this PDF is thus unexplored. Its future exploration with, for example, CHEOPS would be desirable to fully exclude a transiting nature for the planet.


Fig. 8. Same as Fig. 1 for HD 31527 b.

Fig. 10. Same as Fig. 1 for HD 45184 b.

Fig. 9. Same as Fig. 1 for HD 39194 b.

Fig. 11. Same as Fig. 1 for HD 47186 b.

5.8. HD 39194

This star is a $V = 8.1$ early K-dwarf around which HARPS detected three super-Earths with orbital periods of 5.6 d, 14.0 d, and 33.9 d (M11, Queloz et al. in prep.). Our analysis of the updated HARPS dataset (261 RVs vs 133 in the discovery paper) fully confirmed the existence of these planets, and revealed a low-amplitude trend. With a geometric transit probability of $\sim 6.5\%$, the innermost of these planets was an interesting target for our program, and we monitored one of its transit windows with *Spitzer* in Dec 2012. As shown in Fig. 9, the resulting light curve was flat, our deduced posterior transit probability being of 0.46% (Table 1).

5.9. HD 45184

M11 reported the detection of a Neptune-mass planet on a 5.9 d period around this bright ($V = 6.4$) solar-type star. Based on more than double the HARPS measurements (174 vs 82), our analysis confirms the existence of this planet, while revealing the presence of a second planet of similar mass, $\sim 9.5 M_{\oplus}$, on a outer orbit ($P=13.1$ d), and a trend in the RVs that we could relate to the magnetic cycle of the star (Udry et al. in prep.). We monitored the star

for more than 11hrs with *Spitzer* to search for the transit of HD 45184b. The resulting light curve is flat (Fig. 10), while its precision would have been high enough to detect the searched transit for any plausible composition. We did not explore the latest part of the transit window, leaving a posterior probability of 1.3% that the planet undergoes full transit (Table 1), for a prior geometric probability of 7.7%.

5.10. HD 47186

HD 47186 b is a short-period ($P=4.08$ d) Neptune-mass planet discovered by HARPS in 2009 (Bouchy et al. 2009) around a $V = 7.6$ solar-type star, which is also orbited by a giant planet at a much longer period. Our analysis of the extended HARPS dataset confirmed the existence of these two planets, and enabled us to derive an excellent precision on the time of inferior conjunction of the inner planet (1σ -error of 30 min for our *Spitzer* observations). We searched for its transit within our *Spitzer* cycle 6 program. The resulting flat light curve (Fig. 11) enables us to fully reject the transiting nature of the planet (Table 1).

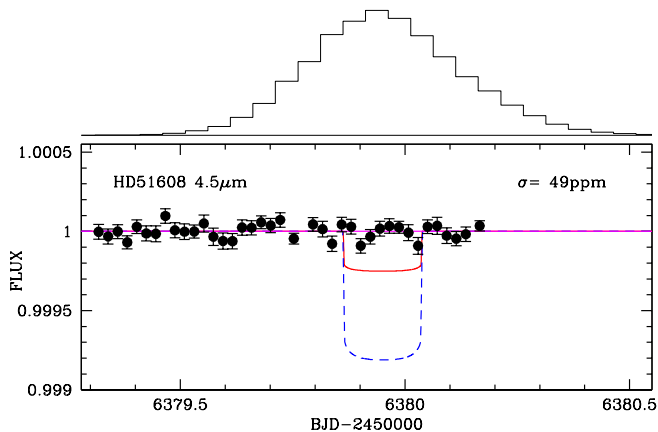


Fig. 12. Same as Fig. 1 for HD 51608 b.

5.11. HD 51608

We used *Spitzer* to search for the transit of the $P = 14.07$ d Neptune-mass planet HD 51608 b detected by M11 around this bright ($V = 6.3$) late G-type dwarf. Our analysis of the updated HARPS dataset (210 RVs) confirmed the existence of the two planets ($P = 14.07$ d and 95 d) announced in M11, and favored a low-amplitude trend of probable magnetic cycle origin (Udry et al. in prep.). Our *Spitzer* photometry (Fig. 12) enabled us to discard a transit of HD 51608 for any plausible planetary composition, our posterior full transit probability being 0.11% (Table 1) for a prior geometric transit probability of $\sim 4\%$.

5.12. HD 93385

The detection of two low-mass planets was reported by M11 for this $V = 7.5$ solar-type star, with derived minimal masses of 8.4 and $10.1 M_{\oplus}$ and orbital periods of 13.2 d and 46 d, respectively. Our analysis of the updated HARPS dataset (231 RVs) revealed the existence of a third lower-mass ($M_p \sin i = 4.0 \pm 0.5 M_{\oplus}$) planet on a 7.3 d orbit (Queloz et al. in prep., see Table A.3). With *Spitzer*, we monitored a transit window (~ 29 hr) of this new planet, HD 93385 d. Our resulting photometry (Fig. 13) did not reveal any clear transit-like structure, and the posterior full transit probability that we derived from its analysis is 0.23% (Table 1), for a prior geometric transit probability of 7.9%. By injecting transit models in this light curve and analyzing the results with our MCMC code, we concluded that its precision of ~ 40 ppm per half-hour is good enough to discard any central transit of a planet with a density equal or smaller than Earth's, but cannot firmly discard the transit of denser planet. We thus recommend the re-observation of the transit window at higher photometrical precision with, for example, CHEOPS.

5.13. HD 96700

HD 96700 b is a $\sim 9 M_{\oplus}$ planet on a 8.1 d orbit discovered by M11 around a $V = 6.5$ solar-type star. Our analysis of the updated HARPS dataset (244 RVs) confirmed its existence and the outer Neptune-mass planet found by M11 on a ~ 100 d period. It also revealed a low-amplitude trend in

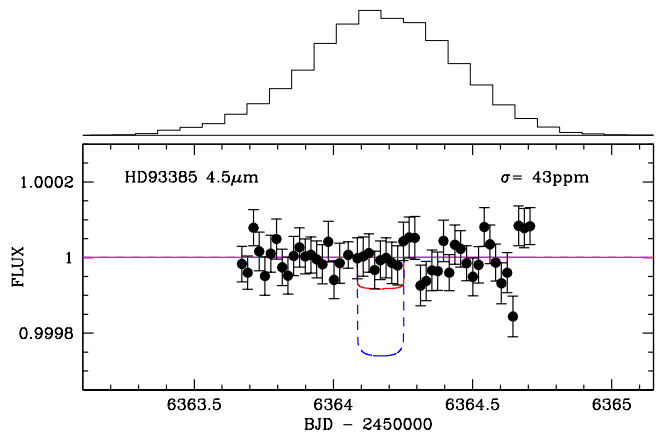


Fig. 13. Same as Fig. 1 for HD 93385 d.

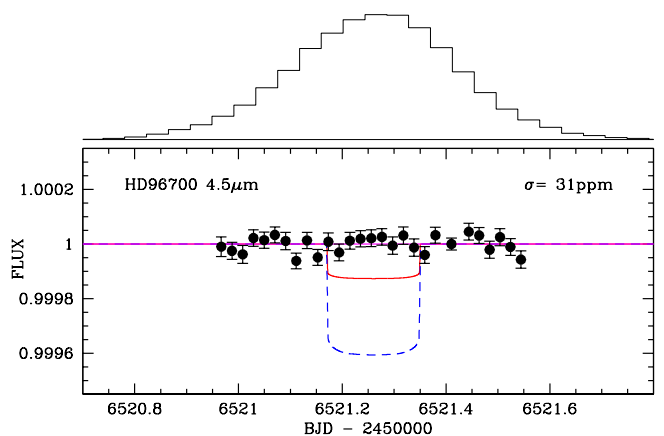


Fig. 14. Same as Fig. 1 for HD 96700 b.

the RVs of probable magnetic cycle origin (Queloz et al. in prep.). We searched for the transit of HD 96700 b with *Spitzer* in 2013, without success (Fig. 14). The precision of the *Spitzer* light curve is high enough to discard a transit of HD 96700 b in it for any possible planetary composition. The resulting posterior transit probability of the planet is 0.09%, for a prior probability of 6.8% (Table 1).

5.14. HD 115617

HD 115617 (aka 61 Vir) is a $V=4.7$ solar-type star (G5V) at only 8.5 pc from Earth. A close-in super-Earth ($M_p \sin i = 5 M_{\oplus}$, $P = 4.215$ d) and two outer Neptunes ($M_p \sin i = 18$ & $23 M_{\oplus}$, $P = 38$ & 123 d) were discovered around it by Vogt et al. (2010) using RVs obtained with Keck/HIRES and the Anglo-Australian Telescope (AAT). We performed a global analysis of the Keck, and AAT RVs that confirmed the existence of the three planets, without revealing any additional object orbiting the star. We used *Spitzer* to observe a transit window of HD 115617 in March 2010.

With $K = 2.96$, HD 115617 is an extremely bright star for *Spitzer*. At $4.5 \mu\text{m}$, it is nevertheless faint enough to be unsaturated for the shortest available integration time (0.01s). However, the *Spitzer* Science Center (SSC) informed us that the requested long observation of HD 115617

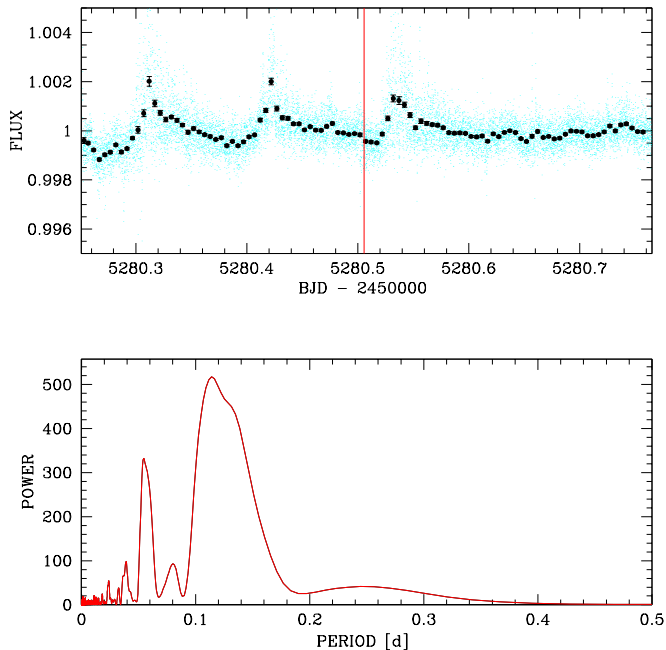


Fig. 15. *Top:* 61 *Vir* light curve obtained by *Spitzer* to search for the transit of its planet b, divided for the best-fit phase-pixel model (here a third order x and y -position polynomial), unbinned (green dots) and binned to intervals of 0.005d (7.2 min). The start of the second AOR is represented by the red vertical line. *Bottom:* Lomb-Scargle periodogram showing a clear power excess at ~ 0.11 days and its first harmonic.

could not be performed at $4.5 \mu\text{m}$ for technical reasons. At $3.6 \mu\text{m}$, the star has a flux density of 19000 ± 4000 mJy while the saturation limit is 20000 mJy for an integration time of 0.01s. SSC informed us the observations could still be performed without any risk of saturation if the star was placed at the corner of four pixels, leading to an effective flux density that was low enough to avoid saturation. We decided to test this strategy. Unfortunately, the light curve corrected for known systematic effects is corrupted by a clear variability at the level of a few tens of percent (Fig. 15, top). A Lomb-Scargle periodogram (Press et al. 1992) of the corrected photometry reveals a power excess at ~ 0.11 days (Fig 15, bottom). We could not identify the origin of this variability. Nevertheless, an astrophysical origin is very unlikely, since HD 115617 is known to be an old inactive star (Vogt et al. 2010). This variability probably originates from the near-saturation of the detector. Indeed, the center of the stellar image was not located at the corner of four pixels as intended. The instrumental effect at work has a typical timescale similar to the signal we are trying to detect, and its amplitude is much larger than the one of the searched transit. Even worse, it seems highly variable in nature and we could not find any analytical function of external parameters (PSF peak value, center position and width, background, etc.) able to represent it satisfactorily. Without a thorough understanding of the effect, we concluded that searching for a transit of a few hundreds of ppm with such data was illusory. The transiting nature of HD 115617b thus remains unconstrained by our project.

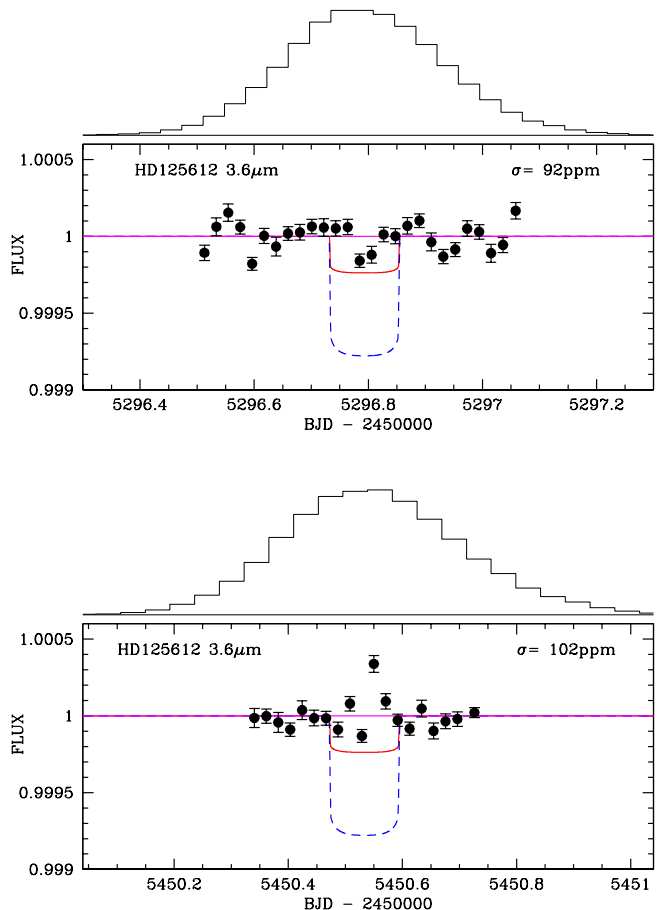


Fig. 16. Same as Fig. 1 for HD 125612 c.

5.15. HD 125612

HD 125612 is a $V = 8.3$ solar-type star around which three planets have been detected so far by RVs, first a $P \sim 510$ d gas giant in 2007 (Fischer et al.) with Keck+HIRES data, then a close-in ($P=4.15$ d) Neptune-mass planet and a ~ 3000 d-period gas giant with HARPS (Lo Curto et al. 2010). In April 2010, we used *Spitzer* to search for the transit of the close-in planet HD 125612 c. Our initial light curve showed a structure consistent with a transit, so we triggered new observations of the transit window with *Spitzer* in September 2010 that did not confirm the transit signal. Reanalyzing the April data, we noticed that the transit signal disappeared when we included terms in the PSF widths, revealing that the signal originated from the *Spitzer* PSF breathing effect (Lanotte et al. 2014). Our global analysis of the two *Spitzer* light curves allowed us to discard a transiting configuration for the planet for any possible planetary composition (Fig. 16), the resulting posterior probability for a full transit being of only 0.24%, for a prior probability of 9.7% (Table 1). We note that the standard deviations of our *Spitzer* light curves binned per 30 min intervals are the largest for HD 125612 (92 and 102 ppm, see Fig. 16). This is also the case for the RV jitter measured from the HARPS RVs (3.2 m s^{-1}), suggesting that HD 125612 is significantly more active star than our other targets.

5.16. HD 134060

HD 134060 is a G0-type dwarf with a V -magnitude of 6.3 at 24pc from Earth, for which M11 and Udry et al. (in prep.) reported the discovery by HARPS of a Neptune (minimal mass = $11 M_{\oplus}$) on a 3.3d orbit, HD 134060 b, in addition to a giant planet on a much wider orbit. Interestingly, the HARPS RVs showed that HD 134060 b has a significant eccentricity of 0.40 ± 0.04 , despite its very short orbit, reminiscent of the still poorly understood eccentricity of the hot Neptune prototype GJ 436 b (Lanotte et al. 2014). Our analysis of the updated HARPS dataset confirmed this significant eccentricity. The orientation of the elliptic orbit of the planet made its occultation by its host star much more likely than its transit (23 vs 8%, see Table A.4), and its timing much better constrained. We thus decided to use a few hours of *Spitzer* first to try to detect the occultation of the planet. We choose to perform the measurement at $3.6\mu\text{m}$, based on the clear detection of the occultation of GJ 436 b at $3.6\mu\text{m}$ and its non-detection at $4.5\mu\text{m}$ (Stevenson et al. 2010, Lanotte et al. 2014). Assuming black-body spectra for the star and the planet, we estimated the expected occultation depth to range from a few tens to more than 200ppm, depending on the unknown planet’s size, albedo, and heat-distribution efficiency. The resulting light curve (Fig. 17, bottom panel) did not reveal a single eclipse, but its precision was not high enough to discard an occultation of the planet for a large range of the plausible planetary parameters cited above. We then attempted a transit search, this time at $4.5\mu\text{m}$. The resulting light curve was flat (Fig. 17, top panel) and enabled us to fully discard a full transit of the planet (Table 1).

5.17. HD 181433

Three planets were detected by HARPS around this $V = 8.4$ K-dwarf (Bouchy et al. 2008). Our analysis of the updated HARPS dataset confirmed the existence of these three planets, and resulted in a prior transit probability of 5% for the inner most of them, the super-Earth HD 181433 b ($M_p \sin i \sim 7.5 M_{\oplus}$, $P=9.375\text{d}$). Our *Spitzer* observations of one of its transit windows led to a transit light curve that did not reveal any transit signature (Fig. 18), while being precise enough to discard a transit for any possible composition of the planet. Our global MCMC analysis of the RVs and *Spitzer* photometry led to a posterior full transit probability of 0.52% (Table 1), which is probably large enough to justify a future exploration of the first part of the transit window that was left unexplored by our *Spitzer* observations (see Fig. 18).

5.18. HD 215497

Two planets were detected by HARPS around this nearby (~ 44 pc) K-dwarf (Lo Curto et al. 2010), one of them being a giant planet on a significantly eccentric 568d-orbit, and the other being a close-in ($P = 3.93\text{d}$) super-Earth ($M_p \sin i = 6 M_{\oplus}$). Our analysis of the updated HARPS dataset, containing only three additional RVs, confirmed the existence of both planets. Based on its interestingly high transit probability of $\sim 12\%$ the inner super-Earth HD 215497 b, we targeted it in our *Spitzer* transit search. The resulting light curve did not reveal any transit signature and was precise enough to discard a transit for most

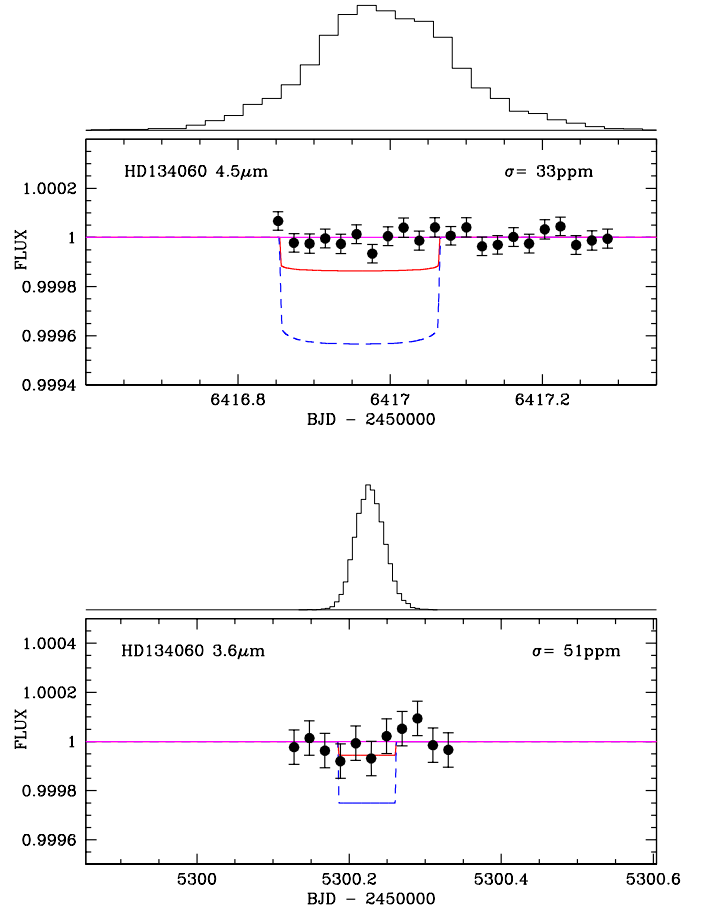


Fig. 17. *Top:* same as Fig. 1 for HD 134060 b. *Bottom:* same for the planet’s occultation. The red solid line and blue dashed line show, respectively, models for a central occultation of a $1.85 R_{\oplus}$ (Earth-like composition) and $5 R_{\oplus}$ (H-dominated composition) planet, assuming a null albedo, an inefficient heat distribution to the night side, and negligible tidal effects for the planet, and assuming black-body emissions for both the planet and its star. The time range of both panels correspond to the same duration so as to outline the fact that the transit timing was much less constrained by the RVs than the occultation timing.

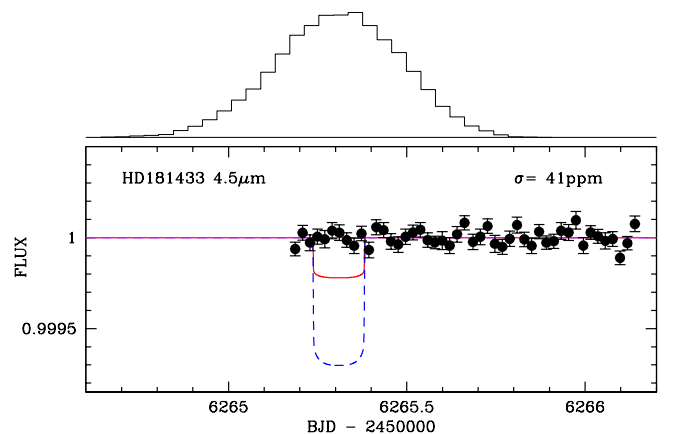


Fig. 18. Same as Fig. 1 for HD 181433 b.

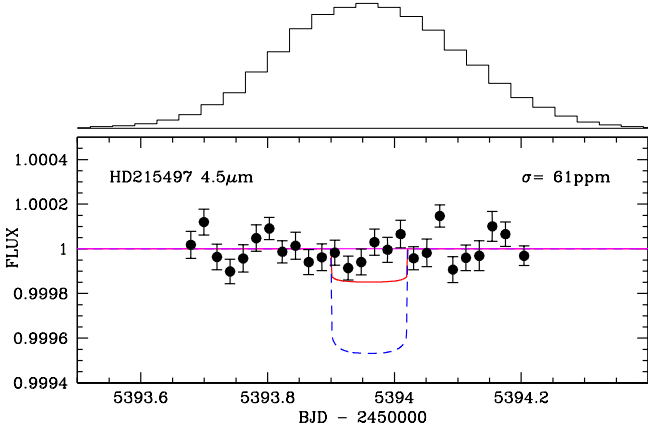


Fig. 19. Same as Fig. 1 for HD 215497 b.

plausible compositions. Yet, a high impact parameter transit of an iron-dominated planet is not discarded by the data (see Fig. 19), resulting in a small but significant posterior full transit probability of $\sim 0.31\%$ (Table 1).

5.19. HD 219828

Discovered by Melo et al. in 2007, HD 219828 b is a hot Neptune ($M_p \sin i = 20M_\oplus$) with an interestingly high geometric transit probability of $\sim 14\%$, thanks to its close-in orbit ($a=0.05$ au, $P=3.83$ d), combined with the relatively large size of its evolved G0-type host star ($R_* = 1.6R_\odot$). On the other hand, this large stellar size translated in expected transit depths as small as 100 ppm (pure iron composition), so we monitored two transit windows to reach a photometric precision that was high enough to firmly constrain the (non-)transiting nature of the planet. The resulting light curves, both obtained at $4.5 \mu\text{m}$, are shown in Fig. 20. They do not reveal any transit signature. Our global analysis of the RVs + photometry led to a complete rejection of a full transit configuration (Table 1-). Our analysis of the much extended HARPS dataset compared to the HD 219828 b discovery paper (91 vs 22 RVs) confirmed the existence of a second, more massive planet ($M_p \sin i \sim 15M_{Jup}$) planet on a very eccentric ($e = 0.81$) long-period ($P=13.1$ years) orbit, as recently announced by Santos et al. (2016).

6. Discussion and conclusion

The constraint brought by the *Spitzer* photometry on the transiting nature of a given planet can be directly estimated in Table 1 by comparing the derived prior and posterior transit probabilities. For 16 out of the 19 RV planets targeted here, our *Spitzer* observations explored the transit window with a coverage and precision high enough to make a transiting configuration very unlikely, the posterior transit probabilities for these 16 targets all being less than 0.55% (Table 1). For HD 45184 b, this posterior transit probability is still of 1.3%, because our *Spitzer* observations did not explore the second part of its transit window (see Sect. 5.9 and Fig. 10). The transiting nature of HD 13808 b and HD 115617 b is left unexplored by our observations.

For the radius of each planet, our MCMC analysis assumed a uniform prior PDF ranging from a pure-iron com-

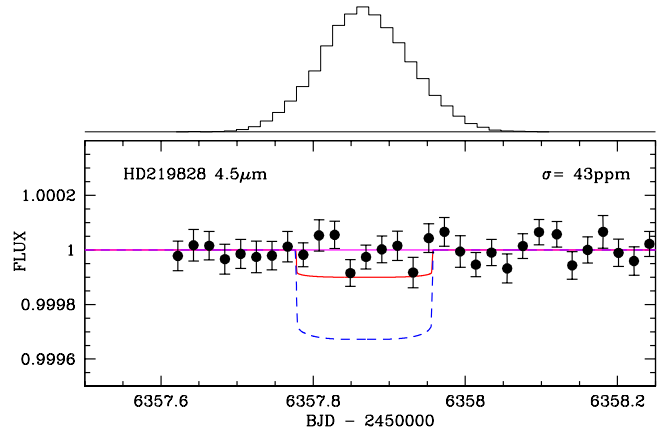
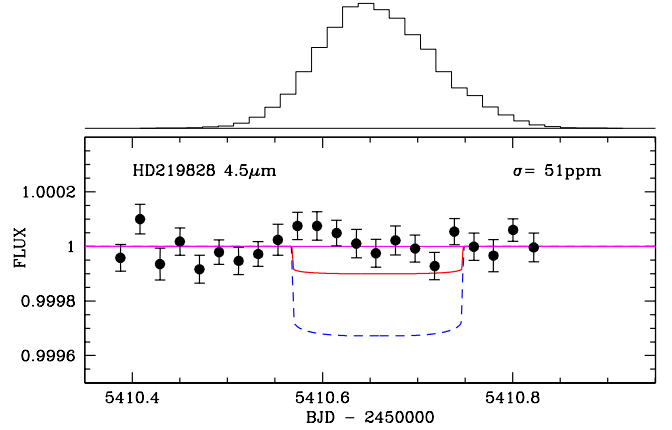


Fig. 20. Same as Fig. 1 for HD 219828 b.

position radius to $11 R_\oplus$. The fact that a transiting configuration was disfavored by our MCMC analysis for all targeted planets does not preclude the possibility that one or several transits were in the data, but were just too shallow to be noticed by the Markov Chains. To estimate the actual detection threshold of our observations, we performed the following procedure for each of our targets. We created 50 fake transit light curves based on the multiplication of the actual light curve by a transit model of the targeted RV planets, each transit assuming a circular orbit for the planet, a mid-transit time drawn from the prior transit timing PDF, which was derived from the RV analysis, and an impact parameter drawn from a uniform PDF that ranged from 0 to 0.9. For each transit model, the depth was automatically tuned to have a difference in BIC of +9.2 between models neglecting and taking into account the transit. This difference in BIC corresponds to a Bayes factor of $e^{9.2/2} = 100$, indicating a decisive selection of the transit model (Jeffreys 1961), i.e. a firm detection (at better than 3-3.5 sigma) of the transit. We then averaged the transit depths (and planet's radii) derived for the 50 light curves and adopted the resulting value as the detection threshold for the considered dataset. These detection thresholds are given in Table 1, expressed as transit depth (in ppm) and planetary radius. For each planet, they are compared to the planet's radius assuming pure-iron and Earth-like compositions. The detection threshold radius is smaller than the ones assuming pure-iron and Earth-like compositions for,

respectively, 5 and 14 of the 17 planets for which the transiting nature was constrained by our observations. For 12 and 3 planets, we cannot thus fully reject the absence of a transit in our data, provided very metal-rich and Earth-like compositions, respectively. However, no transiting configuration is even mildly favored for any planet by our MCMC analysis (from the comparison of the last columns of Table 1), so, considering the excellent photometric precision of our *Spitzer* data, the hypothesis of a missed transit is clearly unlikely. Using the posterior transit probabilities shown in Table 1, the formula $1 - \prod_{i=1:19} P_i(tr, D)$ indeed results in a posterior probability that none of the probed 19 planets transits of 83%, vs 22% for the corresponding prior probability ($1 - \prod_{i=1:19} P_i(tr)$).

Our multi-Cycle *Spitzer* transit search explored the transiting nature of 25 RV planets. It detected one or several transits for the planets HD 75732 e (aka 55 Cnc e) (Demory et al. 2011, Gillon et al. 2012) and HD 219234 b (Motalebi et al 2015), confirmed the transiting nature of HD 97658 b (Van Grootel et al. 2015), discarded or disfavored the transiting nature of 20 planets (including one presented in Ségransan et al., in prep.), and left the one of two planets unconstrained. By discovering the transits of two planets of a few Earth-masses that are suitable for detailed atmospheric characterization, it brought a significant contribution to the study of super-Earths. Statistically speaking, its final result is normal: considering all the planets listed in Table 1 except HD 97658 b, which we decided to observe only because we knew that it was probably transiting (Dragomir et al. 2013), the sum of the geometric transit probabilities amounts to 196%, i.e. the project was expected to observe the transits of ~ 2 planets.

The photometric performances demonstrated by *Spitzer* in this program are illustrated in Fig. 21. This figure compares as a function of the targets' K -magnitude the standard deviations measured in the detrended light curves for a sampling of 30 min to the corresponding formal errors computed following the instructions of the *Spitzer* Observation Manual (SOM⁶). At $4.5\mu\text{m}$, the measured standard deviations are well modeled by the linear relationship $\sigma_{30min} = 32.5 + 11.97 \times (K_{mag} - 5)$ ppm, while the mean quadratic difference between the measured standard deviations and the formal errors is 35 ± 5 ppm. This quadratic difference is 64 ± 9 ppm at $3.6\mu\text{m}$, and 45 ± 4 ppm when neglecting HD125612, which seems to be a more active star than our other targets (Sec. 5.15). These quadratic differences can be attributed to the low-frequency noise of instrumental and astrophysical origins that cannot be represented by our instrumental model. Figure 21 shows that this red noise dominates the photometric precision of *Spitzer*, especially for the brighter targets. Its values are low enough – a few dozens of ppm – to qualify the photometric precision of *Spitzer* as excellent, and to make it an optimal facility for the search for very low-amplitude transits on bright nearby stars.

The *Spitzer* mission should come to an end in early 2019. Fortunately, the CHEOPS space mission (Broeg et al. 2015) will arrive just in time to take over the search for the transits of super-Earths discovered by RVs around nearby stars. CHEOPS will not benefit from a targets' visibility as favorable as *Spitzer*, but its full dedication to transit

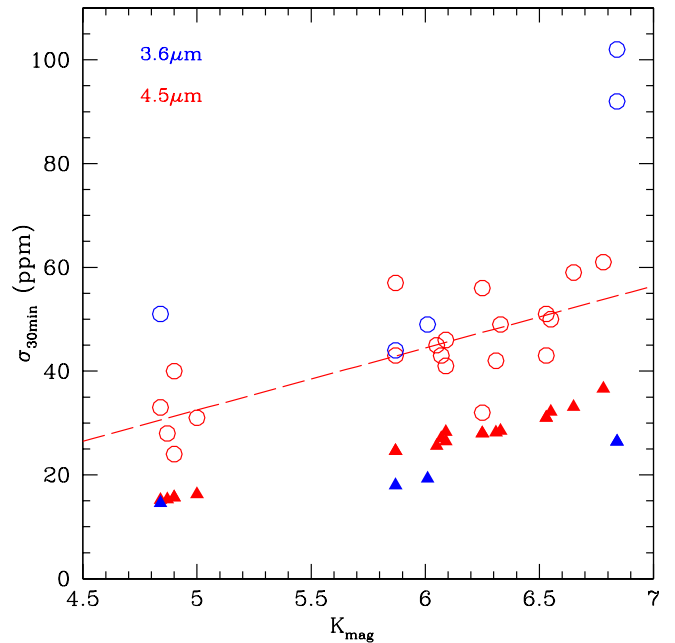


Fig. 21. Standard deviations of the detrended *Spitzer* photometry binned per 30 min (open circles) and the corresponding formal errors (triangles) as a function of the K -magnitude of the targets. Blue = $3.6\mu\text{m}$, red = $4.5\mu\text{m}$. The dashed red line shows the best-fit linear relationship between the standard deviations measured at $4.5\mu\text{m}$ and the K -magnitudes, its equation being $\sigma_{30min} = 32.5 + 11.97 \times (K_{mag} - 5)$ ppm.

observations will more than compensate for its geocentric orbit.

Acknowledgements. This work is based in part on observations made with the *Spitzer Space Telescope*, which is operated by the Jet Propulsion Laboratory, California Institute of Technology under a contract with NASA. Support for this work was provided by NASA. M. Gillon is Research Associate at the Belgian Scientific Research Fund (F.R.S-FNRS). This publication makes use of data products from the Two Micron All Sky Survey, which is a joint project of the University of Massachusetts and the Infrared Processing and Analysis Center/California Institute of Technology, funded by the National Aeronautics and Space Administration and the National Science Foundation.

References

- Arriagada, P., Anglada-Escudé, G., Butler, R. P., et al. 2013, *ApJ*, 771, 42
- Baranne, A., Queloz, D., Mayor, M. et al. 1996, *A&AS*, 119, 373
- Bonfils, X., Gillon, M., Forveille, T., et al. 2011, *A&A*, 528, A111
- Bouchy F., Mayor M., Lovis C., et al., 2009, *A&A*, 496, 527
- Broeg, C., Fortier, A., Ehrenreich, D., et al. 2013, *Hot Planets and Cool Stars*, Garching, Germany, Edited by Roberto Saglia; EPJ Web of Conferences, Volume 47
- Butler, R. P., Vogt, S. S., Marcy, G. W., et al. 2004, *ApJ*, 617, 580
- Casagrande, L., Schoenrich, R., Asplund, M., et al. 2011, *A&A*, 530, 138
- Charbonneau, D., Berta, Z. K., Irwin, J., et al. 2009, *Nature*, 462, 891
- Claret, A. 2000, *A&A*, 363, 1081
- Claret, A., & Bloemen, S. 2011, *A&A*, 529, A75
- Demory, B.-O., Gillon, M., Deming, D., et al. 2011, *A&A*, 533, A114
- Demory, B.-O., Gillon, M., Seager, S., et al. 2012, *ApJL*, 751, 28
- Díaz, R. F., Ségransan, D., Udry, S., et al. 2016, *A&A*, 585, A134
- Dragomir, D., Matthews, J. M., Eastman, J. D., et al. 2013, *ApJL*, 772, 2

⁶ <http://ssc.spitzer.caltech.edu/warmmission/propkit/som/>

Planet	M_s	d	K	$M_p \sin i$	Detection threshold	Pure-Fe radius	Earth-like radius	Prior $P(tr)$	Posterior $P(tr, D)$
	$[M_\odot]$	[pc]		$[M_\oplus]$	ppm/ $[R_\oplus]$	$[R_\oplus]$	$[R_\oplus]$	[%]	[%]
HD 40307 b ¹	0.78	12.8	4.79	4.3	150/0.91	1.13	1.44	6.6	0.19
GJ 3634 b ²	0.45	19.8	7.47	7.0	500/1.05	1.31	1.65	7.0	0.50
HD 75732 e ^{3,4}	0.91	12.3	4.02	7.8	NA ^a	1.34	1.70	28.9	100
HD 97658 b ⁵	0.77	21.1	5.73	7.6	NA ^a	1.33	1.69	4.3	100
HD 219134 b ⁶	0.78	6.5	5.57	4.3	NA ^a	1.15	1.44	9.5	100
BD-061339 b ⁷	0.63	20.3	6.31	6.9	235/1.15	1.30	1.64	7.7	0.53
HD1461 b ⁷	1.04	23.2	4.90	6.7	170/1.56	1.29	1.63	8.1	0.14
HD 10180 c ⁷	1.06	39.0	5.87	13.1	180/1.73	1.53	1.95	8.4	0.14
HD 13808 b ⁷	0.77	28.6	6.78	11.8	NA ^a	1.50	1.90	3.5	3.5
HD 20003 b ⁷	0.91	43.8	6.65	11.8	280/1.79	1.49	1.90	3.4	0.54
HD 20781 b ⁷	0.83	35.4	6.55	2.1	220/1.39	0.93	1.17	7.1	0.15
HD 31527 b ⁷	0.96	38.6	6.05	10.7	190/1.64	1.46	1.85	4.4	0.46
HD 39194 b ⁷	0.72	25.9	6.09	4.1	210/1.22	1.12	1.42	6.4	0.46
HD 45184 b ⁷	1.00	21.9	4.87	12.1	150/1.39	1.50	1.91	7.7	1.29
HD 47186 b ⁷	1.03	39.6	6.01	23.2	175/1.59	1.77	2.26	10.5	0.00
HD 51608 b ⁷	0.86	34.8	6.33	13.1	195/1.39	1.54	1.95	4.0	0.11
HD 93385 d ⁷	1.04	42.2	6.07	4.0	200/1.78	1.11	1.41	7.9	0.23
HD 96700 b ⁷	0.96	25.7	5.00	9.1	155/1.58	1.40	1.77	6.8	0.09
HD 115617 b ⁷	0.94	8.6	2.96	6.2	NA ^a	1.26	1.60	9.4	9.4
HD 125612 c ⁷	1.09	54.2	6.84	19.3	290/1.92	1.69	2.16	9.7	0.24
HD 134060 b ⁷	1.07	24.2	4.84	10.0	165/1.61	1.43	1.82	8.4	0.00
HD 181433 b ⁷	0.86	26.8	6.09	7.5	190/1.26	1.33	1.68	4.9	0.52
HD 215497 b ⁷	0.87	43.6	6.78	6.1	250/1.66	1.26	1.59	11.8	0.31
HD 219828 b ⁷	1.18	72.3	6.53	20.2	155/2.18	1.71	2.19	14.2	0.00

Table 1: 24 of the 25 planets targeted by our *Spitzer* multi-cycle transit search. The first group of 5 planets are the targets for which results were presented previously. The second group of 19 planets are the targets of this work. For each planet, column 6 provides the mean transit detection threshold (in ppm and $[R_\oplus]$), as inferred from injection of transit models in the data (see Sec. 6 for details). Column 7 and 8 give the theoretical radii corresponding, respectively, to a pure-iron and Earth-like compositions. Columns 9 and 10 present the a priori (geometric) and a posteriori (after observation) transit probabilities for the planet. ^aNot Applicable: for HD 13808 b and HD 115617 b (61 Vir b), our observations did not constrain the (non-)transiting configuration, while for HD 75732 e (55 Cnc e), HD 97658 b, and HD 219134 b, a transit was firmly detected in the data. References: ¹: Gillon et al. 2010, ²: Bonfils et al. 2011, ³: Demory et al. 2011, ⁴: Gillon et al. 2012a, ⁵: Van Grootel et al. 2014, ⁶: Motalebi et al. 2015, ⁷: this work.

- Dumusque, X., Pepe, F., Lovis, C., & Latham, D. W., 2015, *ApJ*, 808, 171
- Ehrenreich, D., Bourrier, V., Wheatley, P. J., et al. 2015, *Nature*, 522, 459
- Fazio, G. G., Hora, J. L., Allen, L. E., et al., 2004, *ApJS*, 154, 10
- Fischer, D., Marcy, G., Butler, P., et al. 2007, *ApJ*, 669, 1336
- Flower, P. J. 1996, *ApJ*, 469, 355
- Gelman, A., Rubin, D. 1992, *Statist. Sci.*, 7, 457
- Gillon M., Pont F., Demory B.-O., et al, 2007, *A&A*, 472, L13
- Gillon, M., Deming, D., Demory, B.-O., et al. 2010, *A&A*, 518, A25
- Gillon, M., Demory, B.-O., Benneke, B., et al. 2012a, *A&A*, 539, A28
- Gillon, M., Triaud, A. H. M. J., Fortney, J. J., et al. 2012b, *A&A*, 542, A4
- Gillon, M., Demory, B.-O., Madhusudhan, N., et al. 2014, *A&A*, 563, A21
- Glebocki, R. & Gnacinski, P. 2005, *Catalogue of Stellar Rotational Velocities*, ESA, SP-560, 571
- Gray, R. O., Corbally, C. J., Garrison, R. F., et al. 2003, *AJ*, 126, 2048
- Gray, R. O., Corbally, C. J., Garrison, R. F., et al. 2006, *AJ*, 132, 161
- Hog, E., Fabricius, C., Makarov, V. V., et al. 2000, *A&A*, 355, 27
- Houk, N. & Cowley, A. P. 1975, *Michigan Spectral Survey*, Ann Arbor, Dep. Astron., Univ. Michigan, 1
- Howard, A. W., Marcy, G. W., Bryson, S. T., et al. 2012, *ApJS*, 201, 15
- Ingalls, J. G., Krick J. E., Carey, S. J., et al. 2012, *Proc. SPIE 8442*
- Jeffreys, H. 1961, *The Theory of Probability*, 3rd ed. Oxford University Press.
- Kammer, J. A., Knutson H. A., Howard, A. W., et al. 2014, *ApJ*, 781, 103
- Kharchenko, N. V. 2001, *Kinematika i Fizika Nebesnykh Tel*, 17, 409
- Knutson, H. A., Charbonneau, D., Allen, L. A. et al., 2008, *ApJ*, 673, 526
- Knutson, H. A., Benneke, B., Deming, D. & Homeier, D. 2014a, *Nature*, 505, 66
- Knutson, H. A., Dragomir, D., Kreidberg, L., et al. 2014b, *ApJ*, 794, 155
- Kreidberg, L., Bean, J., Desert, J.-M., et al., 2014, *Nature*, 505, 69
- Lanotte, A. A., Gillon, M., Demory, B.-O., et al. 2014, *A&A*, 572, 73
- Lo Curto G., Mayor, M., Benz, W., et al. 2010, *A&A*, 512, A48

- Lo Curto, G., Mayor, M., Benz, W., et al. 2013, *A&A*, 551, 59
- Lanotte, A., Gillon, M., Demory, B.-O., et al. 2014, *A&A*, 572, 73
- Lovis, C., Ségransan, D., Mayor, M., et al. 2011, *A&A*, 528, A112
- Mandel, J., & Agol, E. 2002, *ApJ*, 580, 171
- Mayor, M., Pepe, F., Queloz, D., et al. 2003, *The Messenger*, 114, 20
- Mayor, M., Marnier, M., Lovis, C., et al. 2011, *A&A* (submitted), arXiv1109.2497
- Melo, C., Santos, N. C., Gieren, W., et al. 2007, *A&A*, 467, 721
- Meschiari, S., Wolf, A. S., Rivera, E. et al., 2009, *PASP*, 121, 1016
- Motalebi, F., Udry, S., Gillon, M., et al. 2015, *A&A*, 584, A72
- Noyes, R. W., Hartmann, L. W., Baliunas, S. L., et al. 1984, *ApJ*, 279, 763
- Press, W. H., Teukolsky, S. A., Vetterling, W. T., Flannery, B. P. 1992, *Numerical Recipes in Fortran 77: The Art of Scientific Computing*, Cambridge University Press
- Queloz, D., Henry, G. W., Sivan, J. P., et al. 2001, *A&A*, 379, 279
- Rafikov R. R., 2006, *ApJ*, 648, 666
- Rivera, E. J., Butler, R. P., Vogt, S. S., et al. 2010, *ApJ*, 708, 1492
- Rowe, J. F., Bryson, S. T., Marcy, G. W., et al. 2014, *ApJ*, 784, 45
- Santos, N. C., Bouchy, F., Mayor, M., et al. 2004, *A&A*, 426, L19
- Santos, N. C., Sousa, S. G., Mortier, A., et al. 2013, *A&A*, 556, A150
- Santos, N. C., Santerne, A., Faria, J. P., et al. 2016, *A&A*, 592, A13
- Schwarz, G. E. 1978, *Annals of Statistics*, 6, 461
- Seager, S., Kuchner, M., Hier-Majumder, C. A., Militzer, B. 2007, *ApJ*, 669, 1279
- Seager, S. 2010, *Exoplanet Atmospheres*, Princeton University Press
- Skrutskie, M. F., Cutri, R. M., Stiening, R., et al. 2006, *AJ*, 131, 1163
- Stevens, D. J. & Gaudi, B. S. 2013, *PASP*, 125, 933
- Stevenson, K. B., Harrington, J., Nymeyer, S., et al. 2010, *Nature*, 464, 1161
- Stevenson, K. B., Harrington, J., Fortney, J., et al. 2012, *ApJ*, 754, 136
- Stetson, P. B. 1987, *PASP*, 99, 111
- Valencia D., Guillot, T., Parmentier, V., Freedman, R. S. 2013, *ApJ*, 775, 10
- Van Grootel, V., Gillon, M., Valencia, D., et al. 2014, *ApJ*, 786, 2
- Van Leeuwen, F. 2007, *A&A*, 474, 653
- Vogt, S. S., Wittenmeyer, R. A., Butler, R. P., et al. 2010, *ApJ*, 708, 1366
- Wisniewski, J. P., Ge, J., Crepp, J. R., et al. 2012, *AJ*, 143, 107
- Winn, J. N., Matthews, J. M., Dawson, R. I., et al. 2011, *ApJ*, 733, L18
- Wright, J. T. 2005, *PASP*, 117, 657

Appendix A: Tables

The following tables describe the targets of this work (Tables A.1 to A.4) and the *Spitzer* observations (Tables A.5 to A.11).

Star	BD-061339	HD 1461	HD 10180	HD 13808	HD 20003
d [parsec]	$20.3 \pm 0.7^{(1)}$	$23.2 \pm 0.3^{(1)}$	$39.0 \pm 0.6^{(1)}$	$28.6 \pm 0.5^{(1)}$	$43.8 \pm 1.2^{(1)}$
V [mag]	$9.67 \pm 0.04^{(2)}$	$6.46 \pm 0.01^{(2)}$	$7.32 \pm 0.01^{(12)}$	$8.38 \pm 0.01^{(2)}$	$8.37 \pm 0.01^{(2)}$
K [mag]	$6.31 \pm 0.02^{(3)}$	$4.90 \pm 0.02^{(3)}$	$5.87 \pm 0.02^{(3)}$	$6.25 \pm 0.02^{(3)}$	$6.65 \pm 0.02^{(3)}$
Spectral type	K7V/M0V ⁽⁴⁾	G3V ⁽⁷⁾	G1V ⁽¹³⁾	K2V ⁽¹³⁾	G8V ⁽¹⁶⁾
T_{eff} [K] ^a	$4040 \pm 50^{(5)}$	$5765 \pm 50^{(8)}$	$5910 \pm 50^{(14)}$	$5035 \pm 50^{(8)}$	$5495 \pm 50^{(8)}$
[Fe/H] [dex]	$-0.07 \pm 0.10^{(5)}$	$0.19 \pm 0.01^{(8)}$	$0.08 \pm 0.01^{(14)}$	$-0.21 \pm 0.02^{(8)}$	$0.04 \pm 0.02^{(8)}$
M_* [M_\odot]	$0.63 \pm 0.03^{(5)}$	$1.04 \pm 0.07^{(8)}$	$1.06 \pm 0.05^{(14)}$	$0.77 \pm 0.06^{(8)}$	$0.91 \pm 0.07^{(8)}$
Bolometric Correction	$-1.07 \pm 0.03^{(6)}$	$-0.082 \pm 0.009^{(6)}$	$-0.058 \pm 0.009^{(6)}$	$-0.290 \pm 0.021^{(6)}$	$-0.140 \pm 0.013^{(6)}$
R_* [R_\odot] ^b	0.69 ± 0.02	1.10 ± 0.02	1.18 ± 0.02	0.81 ± 0.02	0.98 ± 0.02
$\log g$ [cgs]	4.56 ± 0.04	4.37 ± 0.04	4.32 ± 0.03	4.51 ± 0.05	4.41 ± 0.04
RV					
Data	HARPS: 102 ⁽⁴⁾ +10 PFS: 15 ⁽⁵⁾	HARPS: 167 ⁽⁹⁾ +82 ⁽¹⁰⁾ +5 Keck: 144 ⁽¹¹⁾	HARPS: 190 ⁽¹⁴⁾ +63	HARPS: 133 ⁽⁹⁾ +89	HARPS: 104 ⁽⁹⁾ +77
Model	2 Keplerians + linear trend	3 Keplerians + quadratic trend +CCF function	6 Keplerians	2 Keplerians + quadratic trend +CCF function	4 Keplerians
Jitter noise [m s^{-1}]	HARPS: 2.7 PFS: 2.7	HARPS: 1.5 Keck: 2.4 & 1.6 ^e	1.5	1.7	1.4
Planet					
$M_p \sin i$ [M_\oplus]	6.93 ± 0.96	6.73 ± 0.47	13.11 ± 0.62	11.83 ± 0.88	11.79 ± 0.61
Min. R_p [R_\oplus] ^c	1.30 ± 0.05	1.29 ± 0.03	1.53 ± 0.02	1.50 ± 0.03	1.49 ± 0.02
Min. $(R_p/R_*)^2$ [ppm] ^c	298 ± 29	115 ± 6	142 ± 6	286 ± 18	191 ± 9
T_{eq} [K] ^d	796 ± 17	1154 ± 20	1223 ± 18	674 ± 14	836 ± 12
$T_0-2450000$ [BJD _{TDB}]	$6627.48^{+0.18}_{-0.16}$	6549.30 ± 0.12	$5212.837^{+0.059}_{-0.074}$	6537.49 ± 0.26	6538.34 ± 0.36
P [d]	3.87310 ± 0.00037	5.77198 ± 0.00030	5.75931 ± 0.00021	14.1853 ± 0.0019	11.8489 ± 0.0015
$W_{b=0}$ [min]	139 ± 15	218 ± 11	238 ± 10	246 ± 13	388 ± 23
K [m s^{-1}]	3.90 ± 0.52	2.34 ± 0.13	4.51 ± 0.15	3.73 ± 0.20	3.84 ± 0.20
a [AU]	0.04136 ± 0.00066	0.0638 ± 0.0015	0.0641 ± 0.0010	0.1050 ± 0.0028	0.09817 ± 0.00072
e	$0.11^{+0.11}_{-0.08}$	$0.037^{+0.041}_{-0.026}$	$0.045^{+0.037}_{-0.030}$	$0.042^{+0.043}_{-0.029}$	0.377 ± 0.047
ω [deg]	192^{+69}_{-93}	134^{+110}_{-120}	320^{+51}_{-41}	272^{+85}_{-75}	$267.1^{+7.6}_{-8.3}$
Prior $P_{transit}$ [%]	$7.72^{+0.77}_{-0.71}$	8.06 ± 0.38	$8.38^{+0.30}_{-0.33}$	3.52 ± 0.18	3.43 ± 0.15
Prior $P_{occultation}$ [%]	$7.9^{+1.1}_{-0.7}$	8.00 ± 0.38	$8.78^{+0.38}_{-0.32}$	$3.68^{+0.21}_{-0.18}$	$7.50^{+0.62}_{-0.56}$

Table A.1: Targets 1-5 of our *Warm Spitzer* program. For each target, the table presents the assumed stellar parameters, the RV data and details of their analysis, and the parameters that we derived for the planet searched for transit from our RV analysis. ^aFor the sake of realism, a minimal error of 50K was assumed here. ^bFrom luminosity and T_{eff} . ^cAssuming $M_p \sin i = M_p$. These minimum values correspond to a pure iron planet (Seager et al. 2007). ^dAssuming a null albedo and a heat distribution factor $f' = 1/4$ (Seager 2010). ^eFor the first and second Keck datasets presented in Rivera et al. (2010), respectively. References: ⁽¹⁾Van Leeuwen (2007), ⁽²⁾Kharchenko (2001), ⁽³⁾Skrutskie et al. (2006), ⁽⁴⁾Lo Curto et al. (2013), ⁽⁵⁾Arriagada et al. (2013), ⁽⁶⁾Flower (1996), ⁽⁷⁾Gray et al. (2003), ⁽⁸⁾Santos et al. (2013), ⁽⁹⁾Mayor et al. (2011), ⁽¹⁰⁾Díaz et al. (2015), ⁽¹¹⁾Rivera et al. (2010), ⁽¹²⁾Hog et al. (2000), ⁽¹³⁾Gray et al. (2006), ⁽¹⁴⁾Lovis et al. (2011), ⁽¹⁵⁾Queloz et al. in prep., ⁽¹⁶⁾Houk & Cowley (1975), ⁽¹⁷⁾Udry et al. in prep.

Star	HD 20781	HD 31527	HD 39194	HD 45184
d [parsec]	$35.4 \pm 1.3^{(1)}$	$38.6 \pm 0.9^{(1)}$	$21.9 \pm 0.2^{(1)}$	
V [mag]	$8.44 \pm 0.01^{(2)}$	$7.48 \pm 0.01^{(2)}$	$8.08 \pm 0.01^{(2)}$	$6.37 \pm 0.01^{(4)}$
K [mag]	$6.55 \pm 0.02^{(3)}$	$6.05 \pm 0.02^{(3)}$	$6.09 \pm 0.02^{(3)}$	$4.87 \pm 0.02^{(3)}$
Spectral type	K0V ⁽⁴⁾	G0V ⁽⁹⁾	K0V ⁽⁴⁾	G2V ⁽⁴⁾
T_{eff} [K] ^a	$5255 \pm 50^{(5)}$	$5900 \pm 50^{(5)}$	$5205 \pm 50^{(5)}$	$5870 \pm 50^{(5)}$
[Fe/H] [dex]	$-0.11 \pm 0.02^{(5)}$	$-0.17 \pm 0.01^{(5)}$	$-0.61 \pm 0.02^{(5)}$	$0.04 \pm 0.01^{(5)}$
M_* [M_\odot]	$0.83 \pm 0.06^{(5)}$	$0.96 \pm 0.07^{(5)}$	$0.72 \pm 0.05^{(2)}$	$1.00 \pm 0.07^{(5)}$
Bolometric Correction	$-0.208 \pm 0.016^{(6)}$	$-0.059 \pm 0.009^{(6)}$	$-0.225 \pm 0.017^{(6)}$	$-0.058 \pm 0.008^{(6)}$
R_* [R_\odot] ^b	0.86 ± 0.02	1.09 ± 0.02	0.77 ± 0.02	1.04 ± 0.02
$\log g$ [cgs]	4.49 ± 0.04	4.35 ± 0.04	4.52 ± 0.04	4.40 ± 0.04
RV				
Data	HARPS: 96 ⁽⁷⁾ +117	HARPS: 167 ⁽⁷⁾ +75	HARPS: 133 ⁽⁷⁾ +128	HARPS: 82 ⁽⁷⁾ +92
Model	4 Keplerians	3 Keplerians	3 Keplerians + quadratic trend + CCF function	2 Keplerians + quartic trend + CCF function
Jitter noise [m s^{-1}]	1.2	1.2	1.1	1.95
Planet	HD 20781 b ⁽⁸⁾	HD 31527 b ^(7,8)	HD 39194 b ^(7,9)	HD 45184 b ^(7,8)
$M_p \sin i$ [M_\oplus]	2.12 ± 0.35	10.68 ± 0.71	4.08 ± 0.32	12.08 ± 0.86
Min. R_p [R_\oplus] ^c	0.93 ± 0.04	1.46 ± 0.03	1.12 ± 0.03	1.50 ± 0.03
Min. $(R_p/R_*)^2$ [ppm] ^c	99 ± 11	150 ± 8	179 ± 13	175 ± 10
T_{eq} [K] ^d	993 ± 20	839 ± 15	935 ± 19	1143 ± 20
T_0 -2450000 [BJD _{TDB}]	6613.92 ± 0.23	6792.65 ± 0.36	6285.93 ± 0.15	6317.67 ± 0.13
P [d]	5.3144 ± 0.0011	16.5547 ± 0.0033	5.63675 ± 0.00044	5.88607 ± 0.00032
$W_{b=0}$ [min]	180 ± 6	293 ± 19	174 ± 10	209 ± 13
K [m s^{-1}]	0.88 ± 0.14	2.78 ± 0.13	1.83 ± 0.12	4.33 ± 0.23
a [AU]	0.0560 ± 0.0014	0.1253 ± 0.0031	0.0555 ± 0.0013	0.0638 ± 0.0015
e	0 (fixed)	0.117 ± 0.052	$0.033^{+0.035}_{-0.023}$	$0.122^{+0.053}_{-0.057}$
ω [deg]	-	42^{+23}_{-26}	224^{+97}_{-90}	178^{+30}_{-27}
Prior $P_{transit}$ [%]	7.14 ± 0.25	4.40 ± 0.29	6.38 ± 0.36	$7.72^{+0.51}_{-0.44}$
Prior $P_{occultation}$ [%]	7.14 ± 0.25	3.81 ± 0.22	$6.57^{+0.42}_{-0.33}$	$7.67^{+0.48}_{-0.43}$

Table A.2: Same as Table A.1 for targets 6-9. References: ⁽¹⁾Van Leeuwen (2007), ⁽²⁾Hog et al. (2000), ⁽³⁾Skrutskie et al. (2006), ⁽⁴⁾Kharchenko (2001), ⁽⁵⁾Santos et al. (2013), ⁽⁶⁾Flower (1996), ⁽⁷⁾Mayor et al. (2011), ⁽⁸⁾Udry et al. in prep., ⁽⁹⁾Queloz et al. in prep.

Star	HD 47186	HD 51608	HD 93385	HD 96700	HD 115617
d [parsec]	$39.6 \pm 1.0^{(1)}$	$34.8 \pm 0.7^{(1)}$	$42.2 \pm 1.3^{(1)}$	$25.7 \pm 0.4^{(1)}$	$8.56 \pm 0.02^{(1)}$
V [mag]	$7.63 \pm 0.01^{(2)}$	$8.17 \pm 0.01^{(2)}$	$7.49 \pm 0.01^{(2)}$	$6.50 \pm 0.01^{(2)}$	$4.73 \pm 0.01^{(4)}$
K [mag]	$6.01 \pm 0.03^{(3)}$	$6.33 \pm 0.02^{(3)}$	$6.07 \pm 0.02^{(3)}$	$5.00 \pm 0.02^{(3)}$	$2.96 \pm 0.24^{(3)}$
Spectral type	G5V ⁽⁴⁾	G7V ⁽⁴⁾	G2/G3V ⁽⁴⁾	G1/G2V ⁽⁴⁾	G5V ⁽⁴⁾
T_{eff} [K] ^a	$5675 \pm 50^{(5)}$	$5360 \pm 50^{(5)}$	$5975 \pm 50^{(5)}$	$5845 \pm 50^{(5)}$	$5575 \pm 50^{(5)}$
[Fe/H] [dex]	$0.23 \pm 0.02^{(5)}$	$-0.07 \pm 0.01^{(5)}$	$0.02 \pm 0.01^{(5)}$	$-0.18 \pm 0.01^{(5)}$	$0.01 \pm 0.05^{(5)}$
M_* [M_\odot]	$1.03 \pm 0.07^{(5)}$	$0.86 \pm 0.06^{(5)}$	$1.04 \pm 0.07^{(5)}$	$0.96 \pm 0.07^{(5)}$	$0.94 \pm 0.08^{(5)}$
Bolometric Correction	$-0.100 \pm 0.010^{(6)}$	$-0.176 \pm 0.016^{(6)}$	$-0.049 \pm 0.007^{(6)}$	$-0.069 \pm 0.008^{(6)}$	$-0.120 \pm 0.012^{(6)}$
R_* [R_\odot] ^c	1.10 ± 0.02	0.91 ± 0.02	1.15 ± 0.02	1.16 ± 0.02	0.98 ± 0.02
$\log g$ [cgs]	4.37 ± 0.04	4.45 ± 0.04	4.33 ± 0.04	4.29 ± 0.04	4.43 ± 0.05
RV					
Data	HARPS: 66 ⁽⁷⁾ +67	HARPS: 118 ⁽⁸⁾ +92	HARPS: 127 ⁽⁸⁾ +106	HARPS: 146 ⁽⁸⁾ +98	AAT: 126 ⁽¹⁰⁾ + Keck: 80 ⁽¹⁰⁾
Model	2 Keplerians	2 Keplerians + quadratic trend + CCF function	3 Keplerians	2 Keplerians + quadratic trend + CCF function	3 Keplerians
Jitter noise [m s^{-1}]	0.9	1.2	1.3	1.6	Keck: 2.3 AAT: 2.2
Planet					
$M_p \sin i$ [M_\oplus]	23.2 ± 1.1	13.12 ± 0.77	3.97 ± 0.48	9.05 ± 0.64	5.86 ± 0.66
Min. R_p [R_\oplus] ^c	1.77 ± 0.02	1.54 ± 0.02	1.11 ± 0.03	1.40 ± 0.02	1.24 ± 0.04
Min. $(R_p/R_*)^2$ [ppm] ^c	217 ± 9	239 ± 13	79 ± 7	121 ± 6	135 ± 9
T_{eq} [K] ^d	1277 ± 22	749 ± 14	1129 ± 19	1087 ± 19	1190 ± 24
T_0 -2450000 [BJD _{TDB}]	5179.972 ± 0.021	$6379.95^{+0.18}_{-0.16}$	6364.17 ± 0.27	6521.26 ± 0.16	5280.71 ± 0.17
P [d]	4.084575 ± 0.000043	14.0702 ± 0.0015	7.3422 ± 0.0014	8.12541 ± 0.00068	4.21504 ± 0.00061
$W_{b=0}$ [min]	190 ± 6	255 ± 11	227^{+20}_{-24}	273^{+16}_{-13}	174 ± 9
K [m s^{-1}]	9.1 ± 1.3	3.85 ± 0.14	4.51 ± 0.15	2.97 ± 0.15	2.44 ± 0.24
a [AU]	0.0505 ± 0.0012	0.1084 ± 0.0025	0.0749 ± 0.0017	0.0780 ± 0.0019	0.0500 ± 0.0014
e	0.039 ± 0.014	$0.033^{+0.033}_{-0.023}$	$0.13^{+0.10}_{-0.09}$	$0.049^{+0.049}_{-0.034}$	$0.078^{+0.083}_{-0.055}$
ω [deg]	57 ± 23	130^{+74}_{-66}	87 ± 60	293 ± 74	58^{+73}_{-160}
Prior $P_{transit}$ [%]	10.45 ± 0.34	$3.97^{+0.19}_{-0.16}$	$7.9^{+1.1}_{-0.7}$	$6.76^{+0.33}_{-0.36}$	$9.45^{+0.99}_{-0.63}$
Prior $P_{occultation}$ [%]	9.84 ± 0.31	3.84 ± 0.17	$6.68^{+0.54}_{-0.61}$	$7.12^{+0.45}_{-0.34}$	$8.89^{+0.63}_{-0.72}$

Table A.3: Same as Table A.1 for targets 10-14. References: ⁽¹⁾Van Leeuwen (2007), ⁽²⁾Hog et al. (2000), ⁽³⁾Skrutskie et al. (2006), ⁽⁴⁾Kharchenko (2001), ⁽⁵⁾Santos et al. (2013), ⁽⁶⁾Flower (1996), ⁽⁷⁾Bouchy et al. (2009), ⁽⁸⁾Mayor et al. (2011), ⁽⁹⁾Udry et al. in prep., ⁽¹⁰⁾Queloz et al. in prep., ⁽¹¹⁾Vogt et al. (2010)

Star	HD 125612	HD 134060	HD 181433	HD 215497	HD 219828
d [parsec]	$54.2 \pm 3.0^{(1)}$	$24.2 \pm 0.3^{(1)}$	$26.8 \pm 0.8^{(1)}$	$43.6 \pm 2.0^{(1)}$	$72.3 \pm 3.9^{(1)}$
V [mag]	$8.32 \pm 0.02^{(2)}$	$6.29 \pm 0.01^{(2)}$	$8.38 \pm 0.01^{(4)}$	$8.95 \pm 0.02^{(2)}$	$8.01 \pm 0.01^{(2)}$
K [mag]	$6.84 \pm 0.03^{(3)}$	$4.84 \pm 0.03^{(3)}$	$6.09 \pm 0.02^{(3)}$	$6.78 \pm 0.02^{(3)}$	$6.53 \pm 0.02^{(3)}$
Spectral type	G3V ⁽⁴⁾	G3IV ⁽⁴⁾	K5V ⁽⁴⁾	K3V ⁽⁴⁾	G0IV ⁽⁴⁾
T_{eff} [K] ^a	$5915 \pm 50^{(5)}$	$5965 \pm 50^{(5)}$	$4880 \pm 50^{(5)}$	$5000 \pm 100^{(5)}$	$5890 \pm 50^{(5)}$
[Fe/H] [dex]	$0.24 \pm 0.01^{(5)}$	$0.14 \pm 0.01^{(5)}$	$0.36 \pm 0.18^{(5)}$	$0.25 \pm 0.05^{(5)}$	$0.19 \pm 0.03^{(5)}$
M_* [M_\odot]	$1.09 \pm 0.07^{(5)}$	$1.07 \pm 0.07^{(5)}$	$0.86 \pm 0.17^{(5)}$	$0.87 \pm 0.11^{(5)}$	$1.18 \pm 0.08^{(5)}$
Bolometric Correction	$-0.057 \pm 0.008^{(6)}$	$-0.050 \pm 0.007^{(6)}$	$-0.360 \pm 0.024^{(6)}$	$-0.304 \pm 0.048^{(6)}$	$-0.061 \pm 0.008^{(6)}$
R_* [R_\odot] ^a	1.03 ± 0.02	1.15 ± 0.02	0.84 ± 0.02	0.97 ± 0.04	1.60 ± 0.03
$\log g$ [cgs]	4.43 ± 0.03	4.35 ± 0.04	4.51 ± 0.11	4.40 ± 0.08	4.10 ± 0.04
RV					
Data	HARPS: 58 ⁽⁷⁾ +10	HARPS: 100 ⁽⁹⁾ +50	HARPS: 107 ⁽¹¹⁾ +78	HARPS: 105 ⁽⁷⁾ + 3	HARPS: 22 ⁽²¹⁾ +69
Model	Keck: 19 ⁽⁸⁾ 3 Keplerians	2 Keplerians + CCF & logR'(HK) function	3 Keplerians	2 Keplerians + CCF function	2 Keplerians
Jitter noise [m s^{-1}]	HARPS: 3.2 Keck: 4.7	1.3	1.0	1.3	1.5
Planet					
Planet	HD 125612 c ⁽⁷⁾	HD 134060 b ^(9,10)	HD 181433 b ⁽¹¹⁾	HD 215497 b ⁽⁷⁾	HD 219828 b ⁽¹²⁾
$M_p \sin i$ [M_\oplus]	19.3 ± 2.1	9.97 ± 0.60	7.5 ± 1.1	6.11 ± 0.78	20.2 ± 1.2
Min. R_p [R_\oplus] ^c	1.69 ± 0.04	1.43 ± 0.03	1.33 ± 0.06	1.26 ± 0.04	1.71 ± 0.02
Min. $(R_p/R_*)^2$ [ppm] ^c	226 ± 14	130 ± 8	210 ± 18	141 ± 15	96 ± 5
T_{eq} [K] ^d	1269 ± 21	1469 ± 24	753^{+29}_{-23}	1101 ± 39	1596 ± 27
T_0 -2450000 [BJD _{TDB}]	5296.79 ± 0.14	$6416.96^{+0.10}_{-0.09}$	6265.33 ± 0.17	5393.96 ± 0.14	5410.658 ± 0.050
P [d]	4.15514 ± 0.00044	$3.269555^{+0.000092}_{-0.000080}$	9.37518 ± 0.00056	3.93394 ± 0.00065	3.834863 ± 0.000094
$W_{b=0}$ [min]	172^{+12}_{-16}	309 ± 16	227 ± 19	152 ± 19	271 ± 13
K [m s^{-1}]	7.33 ± 0.73	4.69 ± 0.19	2.72 ± 0.13	2.81 ± 0.27	7.43 ± 0.27
a [AU]	0.0520 ± 0.0011	0.0441 ± 0.0010	$0.0822^{+0.0050}_{-0.0058}$	0.0465 ± 0.0020	0.0507 ± 0.0012
e	$0.093^{+0.090}_{-0.064}$	0.480 ± 0.034	0.380 ± 0.041	0.215 ± 0.096	0.063 ± 0.036
ω [deg]	120^{+66}_{-71}	258.5 ± 5.2	198.2 ± 7.1	122 ± 30	228 ± 39
Prior $P_{transit}$ [%]	$9.7^{+1.1}_{-0.7}$	8.39 ± 0.32	$4.93^{+0.49}_{-0.39}$	$11.8^{+1.8}_{-1.4}$	14.18 ± 0.64
Prior $P_{occultation}$ [%]	$8.86^{+0.59}_{-0.69}$	$23.2^{+1.7}_{-1.5}$	$6.25^{+0.64}_{-0.51}$	$8.57^{+0.97}_{-0.87}$	$15.32^{+0.76}_{-0.67}$

Table A.4: Same as Table A.1 for targets 15-19. References: ⁽¹⁾Van Leeuwen (2007), ⁽²⁾Hog et al. (2000), ⁽³⁾Skrutskie et al. (2006), ⁽⁴⁾Kharchenko (2001), ⁽⁵⁾Santos et al. (2013), ⁽⁶⁾Flower (1996), ⁽⁷⁾Lo Curto et al. (2010), ⁽⁸⁾Fischer et al. (2007), ⁽⁹⁾Mayor et al. (2011), ⁽¹⁰⁾Udry et al. in prep., ⁽¹¹⁾Bouchy et al. (2009), ⁽¹²⁾Melo et al. (2007).

Star	BD-061339	HD 1461	HD 10180
Program ID	90072	(1): 80220 ⁽¹⁾ (2): 90072	(1): 60027 (2) & (3): 90072
Observation date	2013-11-30	(1): 2011-08-31 (2): 2013-09-13	(1): 2010-01-16 (2) : 2013-08-10 (3): 2013-09-09
Channel [μm]	4.5	4.5	(1): 3.6 (2) & (3): 4.5
AOR(s) ^a	(S1): 48815616 (1): 48815360 (2): 48815104	(1): 42790656 (S2): 48816128 (2): 48815872	(1): 38139392 (S2): 48596224 (2): 48595968 (S3): 48595712 (3): 48595456 (1): S18.18.0 (2) & (3): S19.1.0
<i>Spitzer</i> pipeline version	S19.1.0	S19.1.0	(1): S18.18.0 (2) & (3): S19.1.0
Exposure time [s]	0.4	0.1	0.1
N_{BCD} ^b	(1):1038 (2): 970	(1): 5548 (2): 3600	(1): 4400 (2) & (3): 3175
Duration [hr]	(1): 7.9 (2): 7.4	(1): 12.9 (2): 8.4	(1): 10.4 (2) & (3): 7.4
Photometric aperture [pixels]	(1) & (2): 3.5	(1) & (2): 3.5	(1): 3 (2): 2.5 (3): 3
Baseline model ^c	(1): $p(w_x + [xy]^2) + \text{BM}$ (2): $p(w_x + w_y + [xy]^2) + \text{BM}$	(1): $p(w_x^2 + w_y^3 + [xy]^3 + l^2) + \text{BM}$ (2): $p(w_x + [xy]^2) + \text{BM}$	(1): $p(t + w_x + w_y^2 + [xy]^2 + l) + \text{BM}$ (2): $p(w_x + [xy]^2 + l^2) + \text{BM}$ (3): $p(w_x + w_y + [xy]^2 + l) + \text{BM}$
Error correction factors ^d	(1): $\beta_w = 0.94, \beta_r=1.21$ (2): $\beta_w = 0.91, \beta_r=1.24$	(1): $\beta_w = 0.97, \beta_r=1.91$ (2): $\beta_w = 0.94, \beta_r=1.34$	(1): $\beta_w = 0.95, \beta_r=1.62$ (2): $\beta_w = 0.97, \beta_r=1.26$ (3): $\beta_w = 0.99, \beta_r=1.42$

Table A.5: Details of our *Warm Spitzer* data and their analysis for targets 1-3. ^aAOR = astronomical observation request = *Spitzer* observing sequence. (S) designates a short pre-run AOR performed to stabilize the pointing and instrument. ^bBCD = Basic Calibrated Data = block of 64 *Spitzer*/IRAC subarray exposures. ^cFor the baseline model, $p(\epsilon^N)$ denotes, respectively, an N -order polynomial function of the logarithm of time ($\epsilon = l$), of the PSF x - and y -positions ($\epsilon = [xy]$), and widths ($\epsilon = w_x$ & w_y). BM=BLISS mapping. ^dsee Sec. 4. References: ⁽¹⁾Kammer et al. (2014).

Star	HD 13808	HD 20003	HD 20781
Program ID	90072	90072	90072
Observation date	(1) 2013-08-15 (2) 2013-08-27	2013-09-01	2013-11-16
Channel [μm]	4.5	4.5	4.5
AOR(s) ^a	(S1): 48814848 (1): 48814592 (S2): 48818176 (2): 48817920	(S): 48408576 (1): 48408320 (2): 48408064 (3): 48407808	(S): 48817664 (1): 48817408 (2): 488817152 (3): 48816896
<i>Spitzer</i> pipeline version	S19.1.0	S19.1.0	(1): S19.1.0
Exposure time [s]	0.4	0.4	0.4
N_{BCD} ^b	(1) & (2): 970	(1) & (2): 1498 (3): 580	(1) & (2): 1367 (3): 580
Duration [hr]	(1) & (2): 7.4	(1) & (2): 11.5 (3): 4.4	(1) & (2): 10.4 (3): 4.4
Photometric aperture [pixels]	(1): 2.75 (2): 3.5	(1) & (2) & (3): 3.5	(1) & (2) & (3): 2.75
Baseline model ^c	(1): $p(w_x + w_y + [xy]^2) + \text{BM}$ (2): $p(w_x^2 + w_y^2 + [xy]) + \text{BM}$	(1): $p(w_x^2 + w_y^2 + [xy]^2) + \text{BM}$ (2): $p(w_x + w_y + [xy]) + \text{BM}$ (3): $p(w_x + w_y + [xy]) + \text{BM}$	(1): $p(w_x + w_y + [xy]^2) + \text{BM}$ (2): $p(w_x^2 + w_y + [xy]^2) + \text{BM}$ (3): $p(w_x + [xy]^2) + \text{BM}$
Error correction factors ^d	(1): $\beta_w = 0.93, \beta_r = 1.00$ (2): $\beta_w = 0.96, \beta_r = 1.55$	(1): $\beta_w = 0.93, \beta_r = 1.30$ (2): $\beta_w = 0.95, \beta_r = 1.12$ (3): $\beta_w = 0.98, \beta_r = 2.03$	(1): $\beta_w = 0.97, \beta_r = 1.06$ (2): $\beta_w = 0.91, \beta_r = 1.14$ (3): $\beta_w = 0.97, \beta_r = 1.31$

Table A.6: Same as Table A.5 for targets 4-6.

Star	HD 31527	HD 39194
Program ID	90072	90072
Observation date	2014-05-13	2012-12-24
Channel [μm]	4.5	4.5
AOR(s) ^a	(S): 50091776 (1): 50091520 (2): 50091264 (3): 50091008	(S): 46914816 (1): 46914560
<i>Spitzer</i> pipeline version	S19.1.0	(1): S19.1.0
Exposure time [s]	0.4	0.1
N_{BCD} ^b	(1) & (2) & (3): 1558	(1): 4890
Duration [hr]	(1) & (2) & (3): 11.9	(1): 11.4
Photometric aperture [pixels]	(1) & (2) & (3) : 3.25	(1): 3.0
Baseline model ^c	(1): $p(w_x^2 + [xy]^2) + \text{BM}$ (2): $p(w_x + w_y + [xy]^2) + \text{BM}$ (3): $p(w_x + w_y^3 + [xy]^2) + \text{BM}$	(1): $p(w_x + w_y + [xy]^2 + l) + \text{BM}$
Error correction factors ^d	(1): $\beta_w = 0.93, \beta_r = 1.19$ (2): $\beta_w = 0.95, \beta_r = 1.20$ (3): $\beta_w = 0.93, \beta_r = 1.38$	(1): $\beta_w = 0.97, \beta_r = 1.15$

Table A.7: Same as Table A.5 for targets 7-8.

Star	HD 45184	HD 47186	HD 51608
Program ID	90072	60027	90072
Observation date	2013-01-24	2009-12-14	2013-03-27
Channel [μm]	4.5	3.6	4.5
AOR(s) ^a	(S): 46917376 (1): 46917120	38065664	(S): 48411392 (1): 48411136 (2): 48410880
<i>Spitzer</i> pipeline version	S19.1.0	S19.1.0	(1): S19.1.0
Exposure time [s]	0.1	0.1	0.4
N_{BCD} ^b	(1): 4880	2115	(1): 1498 (2): 1300
Duration [hr]	(1): 11.4	5	(1): 11.4 (2): 9.9
Photometric aperture [pixels]	(1): 3.25	2.75	(1) & (2): 2.25
Baseline model ^c	(1): $p(w_x^2 + w_y + [xy]^2 + l) + \text{BM}$	$p(w_x^2 + [xy]^2 + l) + \text{BM}$	(1): $p(w_x + w_y + [xy]^2) + \text{BM}$ (2): $p(w_x + w_y + [xy]^2) + \text{BM}$
Error correction factors ^d	(1): $\beta_w = 0.94, \beta_r = 1.54$	(1): $\beta_w = 1.00, \beta_r = 1.61$	(1): $\beta_w = 0.95, \beta_r = 1.14$ (2): $\beta_w = 0.94, \beta_r = 1.12$

Table A.8: Same as Table A.5 for targets 9-11.

Star	HD 93385	HD 96700	HD 115617
Program ID	90072	90072	60027
Observation date	2013-03-12	2013-08-16	2010-03-25
Channel [μm]	4.5	4.5	3.6
AOR(s) ^a	(S): 48407552 (1): 48407296 (2): 48407040 (3): 48406784	(S): 46916864 (1): 46916608 (2): 46916352	(1): 39138816 (2): 39139072
<i>Spitzer</i> pipeline version	S19.1.0	S19.1.0	S19.1.0
Exposure time [s]	0.1	0.1	0.01
N_{BCD} ^b	(1) & (2): 4245 (3): 2325	(1): 4880 (2): 1240	(1): 6600 (2): 6640
Duration [hr]	(1) & (2): 11.9 (3): 5.4	(1): 11.4 (2): 2.9	(1): 6.2 (2): 6.3
Photometric aperture [pixels]	(1) & (2) & (3) : 2.5	(1) & (2): 2.75	(1) & (2): 2.25
Baseline model ^c	(1): $p(w_x + w_y^2 + [xy] + l) + \text{BM}$ (2): $p(w_x + w_y + [xy]) + \text{BM}$ (3): $p(w_x + [xy]^2) + \text{BM}$	(1): $p(w_x + w_y + [xy]^2) + \text{BM}$ (2): $p(w_x + [xy]^2) + \text{BM}$	(1): - (2): -
Error correction factors ^d	(1): $\beta_w = 0.96, \beta_r = 1.00$ (2): $\beta_w = 1.00, \beta_r = 1.10$ (3): $\beta_w = 1.00, \beta_r = 1.85$	(1): $\beta_w = 0.99, \beta_r = 1.36$ (1): $\beta_w = 0.97, \beta_r = 1.65$	(1): - (2): -

Table A.9: Same as Table A.5 for targets 12-14. The HD 115617 photometry is affected by a strong systematic error that prevented any searching for the transit of HD 115617b.

Star	HD 125612	HD 134060	HD 181433
Program ID	60027	(1): 60027 (2): 90072	90072
Observation date	(1): 2010-04-09 (2): 2010-09-10	(1): 2010-04-13 (2): 2013-05-04	2012-12-03
Channel [μm]	3.6	(1): 3.6 (2): 4.5	4.5
AOR(s) ^a	(1): 38110464 (2): 40313600	(1): 38110720 (S2): 46916096 (2): 46915840	(S): 46915584 (1): 46915328 (2): 46915072
<i>Spitzer</i> pipeline version	S18.18.0	(1): S18.18.0 (2): S19.1.0	S19.1.0
Exposure time [s]	0.4	(1): 0.02 (2): 0.1	0.4
N_{BCD} ^b	(1): 1790 (2): 1310	(1): 6200 (2): 4480	(1): 1563 (2): 1498
Duration [hr]	(1): 13.8 (2): 10.2	(1): 6 (2): 11.5	(1): 11.9 (2): 11.4
Photometric aperture [pixels]	(1): 1.75 (2): 1.9	(1): 1.75 (2): 2.25	(1): 3.25 (2): 3.25
Baseline model ^c	(1): $p(w_x^2 + w_y^2 + [xy]^3 + l) + \text{BM}$ (2): $p(t + w_x + w_y^2 + [xy] + l^2) + \text{BM}$	(1): $p(w_x + [xy]^2 + l) + \text{BM}$ (2): $p(w_x^2 + w_y + [xy]^4) + \text{BM}$	(1): $p(w_x + w_y + [xy]^2) + \text{BM}$ (2): $p(w_x + w_y + [xy]^2) + \text{BM}$
Error correction factors ^d	(1): $\beta_w = 0.81, \beta_r = 2.02$ (2): $\beta_w = 0.72, \beta_r = 2.34$	(1): $\beta_w = 1.00, \beta_r = 1.62$ (1): $\beta_w = 0.95, \beta_r = 1.30$	(1): $\beta_w = 0.95, \beta_r = 1.27$ (2): $\beta_w = 0.93, \beta_r = 1.11$

Table A.10: Same as Table A.5 for targets 15-17.

Star	HD 215497	HD 219828
Program ID	90072	60027 & 90072
Observation date	2010-07-16	(1): 2010-08-01 (2): 2013-03-06
Channel [μm]	4.5	4.5
AOR(s) ^a	38701568	(1): 38702336 (2S): 46914304 (2A): 46914048 (2B): 46913792
<i>Spitzer</i> pipeline version	S18.18.0	S19.1.0
Exposure time [s]	0.4	0.4
N_{BCD} ^b	1750	(1): 1440 (2A): 1564 (2B): 448
Duration [hr]	13.4	(1): 11 (2A): 11.9 (2B): 3.4
Photometric aperture [pixels]	3	(1): 2.5 (2A): 3 (2B): 3
Baseline model ^c	$p(w_x + w_y + [xy] + l) + \text{BM}$	(1): $p(w_x + w_y + [xy]^2 + l^2) + \text{BM}$ (2A): $p(w_x + [xy]^2 + l) + \text{BM}$ (2B): $p(w_x + [xy]^2 + l^2) + \text{BM}$
Error correction factors ^d	$\beta_w = 0.95, \beta_r = 1.20$	(1): $\beta_w = 0.93, \beta_r = 1.53$ (2A): $\beta_w = 0.96, \beta_r = 1.01$ (2B): $\beta_w = 0.94, \beta_r = 1.14$

Table A.11: Same as Table A.5 for targets 18-19.